On the uncertainties in hot spot reconstructions and the significance of moving hot spot reference frames

Craig O'Neill

School of Geosciences, University of Sydney, Edgeworth David Building F05, Sydney, NSW 2006, Australia

Now at Department of Earth Sciences, Rice University, MS 126, Houston, Texas 77251–1892, USA (cjoneill@rice.edu)

Dietmar Müller

School of Geosciences, University of Sydney, Edgeworth David Building F05, Sydney, NSW 2006, Australia

Bernhard Steinberger

Bayerisches Geoinstitut, Universität Bayreuth, D-95440 Bayreuth, Germany

Now at Center for Geodynamics, NGU, 7491 Trondheim, Norway

[1] It is widely accepted that substantial relative motion has occurred between the Indo-Atlantic and Pacific hot spots since the Late Cretaceous. At the same time, a fixed Indo-Atlantic hot spot reference frame has been argued for and used since the advent of plate tectonics, implying relatively little motion between the hot spots in this domain since about 130 Ma. Most plumes purported to have caused these hot spots, while being advected in the global-scale mantle flow field, are assumed to move an order of magnitude more slowly than plates. However, the lifetime of a plume may be over ~100 Myr, and the integrated motion of a plume is expected to be significant over these times. The uncertainties inherent in hot spot reconstructions are of a magnitude similar to the expected plume motion, and so any differences between a fixed and moving frame of reference must be discernible beyond the level of these uncertainties. We present a method for constraining hot spot reconstruction uncertainties, similar to that in use for relative plate motion. We use a modified Hellinger criterion of fit for the hot spot problem, using track geometries and radiometric dating, and derive covariance matrices for our Indo-Atlantic rotations for the last 120 Myr. However, any given mantle convection model introduces additional uncertainties into such models, based on its model parameters and starting conditions (e.g., choice of global tomography model, viscosity profile, nature of mantle phase transitions). We use an interactive evolutionary approach, where we constrain the hot spot motion resulting from convection models to fit paleomagnetic constraints, and converge on an acceptable motion solution by varying unknowns over several generations of simulations. Our hot spot motion model shows large motion (5–10°) of the Indo-Atlantic hot spots for times >80 Ma, consistent with available paleomagnetic constraints. The differences between the fixed and moving hot spot reference frames are not discernible over the level of uncertainty in such rotations for times <80 Ma.

1. Introduction

1.1. Hot Spot Reconstructions

[2] The construction of an absolute geographical reference frame for Earth's history is a long-standing goal of the Earth Science community. While relative plate motions provide much information about the geographical relationship of one region to another in the past, this is insufficient for constraining the position of the plates relative to the geographical axis. Paleomagnetic measurements can constrain the latitudinal evolution of the plates relative to the magnetic pole. The problem is that the position of the Earth's axis, and subsequently the magnetic pole which, on average, aligns with it, varies over geological time due to changes in the Earth's moment of inertia, which result from the evolution of density anomalies in the Earth's interior [*Steinberger and O'Connell*, 1997].

[3] An often-used method for reconstructing the position of the plates relative to a mantle frame of reference involves using hot spot tracks [*Duncan and Richards*, 1991; *Morgan*, 1971; *Müller et al.*, 1993]. Here present-day hot spots are supposed to be the surface expression of mantle plumes, which move an order of magnitude slower than the plates. Hence, to a first approximation, these plumes can be considered stationary, and a best fit rotation between the hot spots and the volcanic chains attributed to them can be found, for each considered time [*Müller et al.*, 1993].

[4] There are two major concerns to this approach. First, mantle plumes are not stationary [*Antretter et al.*, 2002; *Molnar and Stock*, 1987; *Steinberger and O'Connell*, 1998; *Tarduno and Cottrell*, 1997], and while this approximation might hold for younger times over which the differences in motion are not discernible, the motions will be important over ~100 Myr timescales [e.g., *Tarduno and Gee*, 1995], which is the range of times we are interested in. The second concern is to how the uncertainties in our knowledge of the hot spot position through time, and the inherent uncertainties in the data we use, will propagate into a rotation uncertainty. These inherent uncertainties include uncertainties in the position of hot spots during the formation of a volcanic ridge, uncertainties in radiometric dates, and complexities in the dynamics of an evolving dynamic volcanic system. The issue of the uncertainties in such absolute plate rotations is rarely addressed [*Andrews and Gordon*, 2003; *Harada*

and Hamano, 2000; *O'Neill et al.*, 2003], and we find this unsatisfactory as the differences between moving and fixed hot spot reference frames need to be resolved at a level above the uncertainties in the rotations.

[5] The purpose of this paper is twofold. Firstly, our aim is to construct an absolute frame of reference based on moving hot spots. This has been attempted before [*Steinberger*, 2000; *Steinberger and O'Connell*, 1998, 2000], and a well-developed modeling approach exists. However, severe constraints limit the usefulness of such models for times over ~70 Myr [*Steinberger and O'Connell*, 1998]. This is unfortunate, as the ages of the oldest tracks we are interested in are as old as ~120 Ma. Nonetheless, such hot spot motion models provide an explanation for the observed discrepancy between the Indo-Atlantic and the Pacific hot spot domains [*Steinberger*, 2000]. In this paper, we extend such modeling back to 120 Ma. The problems in doing so are discussed, and we develop a hybrid hot spot motion model, combining dynamic simulations of plume motion with paleomagnetic and tomographic constraints. We also develop a statistical technique for constraining the uncertainties in hot spot reconstructions. Our motivation is to develop a technique to allow us to combine uncertainties in hot spot and relative plate reconstructions. A well-developed method for constraining the uncertainties in relative plate motions is given by *Chang* [1988]. We review the geometrical framework for this technique, and the criteria of fit used. We extend his analysis to the problem of hot spot-track-based reconstructions.

1.2. Model of Plume Motion

[6] The method we use for modeling plume motion has been described by *Steinberger and O'Connell* [1998, 2000]. The method calculates the flow field of the mantle using a spectral code of *Hager and O'Connell* [1979, 1981]. The flow is driven by mantle density anomalies and imposed plate velocities. We note that imposing plate velocities creates artifacts in the predicted stress field. However, since here we are only concerned with the mantle flow velocity, and not stresses, we regard imposing given surface velocities as most appropriate for the purpose of this paper. The present-day internal density structure of the Earth is determined from global tomographic models [*Grand et al.*, 1997; *Masters et al.*, 2000; *Su et al.*, 1994]. We ignore velocity variations above 200 km depth to exclude lithospheric effects. We vary the empirical seismic

velocity to density conversion factor from model to model, within the bounds 0.1–0.5.

[7] We model the plume as an initially vertical conduit at the assumed initiation age of the hot spot, which is then advected in the global flow field. Given the range of possible variables in these models, and their often poorly constrained nature, we adopt an interactive evolutionary computational approach [*Boschetti and Moresi*, 2001; *Boschetti et al.*, 2003]. Here factors with an inherent uncertainty are allowed to vary within physically plausible parameter ranges. For example, the distribution and magnitude of velocity heterogeneities varies among different tomographic models. While we do not change the distribution, we can vary the magnitude of these anomalies by applying a different density conversion factor to account for the different amplitudes of each model. Similarly, while the viscosity structure of the Earth can be constrained [*Forte and Mitrovica*, 1991; *King*, 1995; *King and Masters*, 1992; *Ricard et al.*, 1989], the uncertainties in its structure vary considerably with depth, and we allow a range of possible values. The resulting hot spot motions vary considerably. We adopt a ranking criterion for each simulation, based on the fit of the hot spot motion to available paleomagnetic constraints, and the present-day tilt of the conduit to available tomographic constraints. Hence, for each generation of models, we select the parameter ranges which result in the best fit to the paleomagnetic constraints, resulting in convergence on acceptable input parameters.

[8] Additional uncertainties in our simulations arise for hot spot reconstructions up to 120 Ma. As pointed out by *Steinberger and O'Connell* [1998], *Conrad and Gurnis* [2003], and *Bunge et al.* [2003], there are severe problems in what are effectively "backward-convection" calculations for times greater than ~70 Myr. The problem is thermal diffusion; this is inherently a forward process. Once heat diffuses in a system, it is impossible to reconstruct it to its previous thermal structure. *Steinberger and O'Connell* [1998] overcome this by ignoring the diffusion term, and just advecting the density anomalies back through time. They showed this approach is valid over times for which diffusion can be neglected (i.e., ~64 Myr). *Conrad and Gurnis* [2003] applied finite element codes with time reversed to reconstruct the mantle density structure back through time. Since a negative thermal diffusion is inherently numerically unstable, they allowed a small positive diffusion in

their backward calculations. They then ran their models forward in time, to check if they could reconstruct their original (i.e., present-day) mantle density structure. They found that if they restricted their backward calculations to times less than 70 Myr, this was possible. For times greater than this, however, the development of thick thermal boundary layers in their models generated new mantle features in the forward simulations. The approach developed by *Bunge et al.* [2003] is an adjoint inverse model, based on a variational approach, where an optimal initial state is found which best fits the observed present state. They found this extremely computationally intensive to implement, and the approach is sensitive to uncertainties in the tomography model from which the observed present state is deduced.

[9] An interesting point is that the effective time of the back-and-forward simulations of *Conrad and Gurnis* [2003] is over ~140 Myr, i.e., the amount of time for the thermal boundary layers to thicken and generate new structures. This thickening is probably an artifact of a positive diffusion back through time, which allows the accumulation of a thick lower boundary layer. The addition of a heat sink as a lower boundary condition in their backward calculation could, for instance, alleviate this feature. In the code we use, this is not such a problem, as we do not explicitly consider thermal boundary layers (i.e., we are not solving the thermal problem); our top and bottom surfaces are defined by viscous layers with preset velocity boundary conditions. While this minimizes the effects of neglecting diffusion, it also means we are not generating thermal boundary layer features.

[10] All approaches to the inverse convection problem incorporate, in some sense, data assimilation to escape an otherwise intractable calculation. Our approach in this paper builds upon the work of *Steinberger and O'Connell* [1998], in using seismic tomography models as an initial condition to the backward calculation, and past plate motions as a surface boundary condition through time. We include a cosine taper filtering of the amplitudes of the higher harmonic degrees of the density field through time to prevent runaway instabilities developing for older times (T. Becker, personal communication, 2002); this is the numerical equivalent to a small positive diffusion in our calculations. We incorporate an interactive evolutionary approach to our modeling, whereby paleomagnetic, geological and tomographic constraints are used in a selective culling
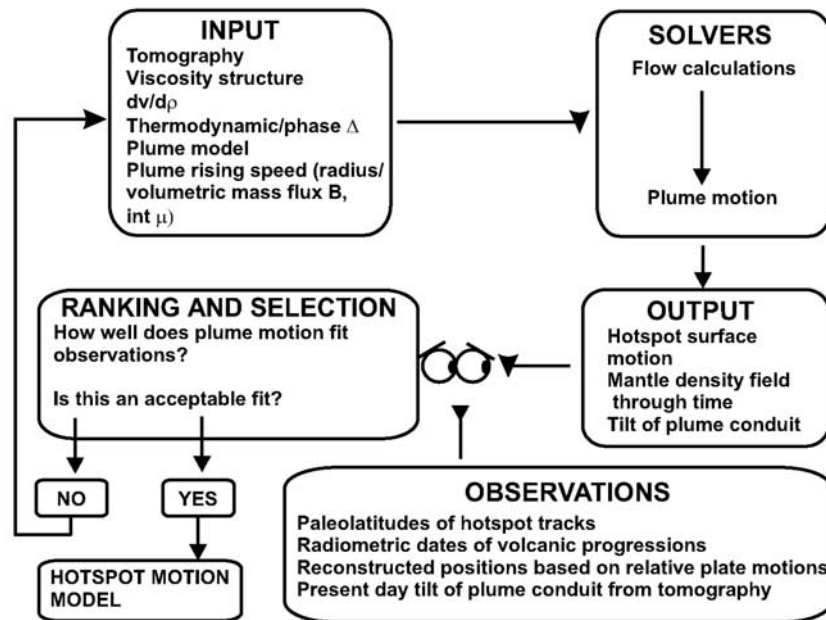
Figure 1. Flowchart of an interactive evolutionary approach to hot spot motion modeling. Input parameters are allowed to vary over physically plausible ranges; these values are used as input to the flow field calculations and calculations of conduit motion in this flow field. The results, surface hot spot motion and present-day conduit tilt, are compared to observational constraints. The results are ranked, and the parameter ranges of the best fit models selected for use in the next generation of simulations. The process is iterated until an acceptable model of hot spot motion is obtained, i.e., one that fits the observational constraints within the limits of their uncertainties.

of each generation of models, and over successive generations of models with varying parameters we converge on an acceptable hot spot motion model. This is shown schematically in Figure 1. It should be noted that the constraints we use on hot spot motion, and present-day conduit tilt, are subject to large uncertainties of their own.

[11] For example, paleomagnetic measurements have their own inherent uncertainties [*McElhinny and McFadden*, 1999], and observed changes in paleolatitudes may be due partly to true polar wander [*Besse and Courtillot*, 2002; *O'Neill et al.*, 2003]. Imaging plume conduits is notoriously difficult due to the assumed small size, and resolution problems [*Montelli et al.*, 2004]. Even of those conduits that appear to have been imaged successfully [*Montelli et al.*, 2004; *Wolfe et al.*, 1997], the conduit structure is still a matter of interpretation. Many plumes cannot be imaged presently due to lack of resolution in those areas. Indeed, comparisons between modeled plume conduit shapes, and those observed, must consider the limitations of the plume model used. Given these issues, we consider an interactive, manual approach

in the ranking and selection of each generation of simulations the best approach.

2. Uncertainties in Hot Spot−Based Reconstructions

2.1. A Modified Hellinger Criterion for Absolute Plate Rotations

[12] The method we adopt for fitting our rotations is similar to that introduced by *Hellinger* [1981] for relative plate rotations. A full description of this is found in Appendix A. However, the general method of fit is not limited to this application. For relative plate rotations, the two data sets, isochrons and fracture zones, essentially describe two orthogonal types of data. Fracture zones are formed by the toroidal motion of two plates relative to one another; they effectively describe the flow lines of one plate relative to the other. Furthermore, they cut across isochrons; i.e., many isochrons can be offset by the same amount by one fracture zone. Isochrons, on the other hand, are constructed from the remanent magnetic signature of the ocean crust.
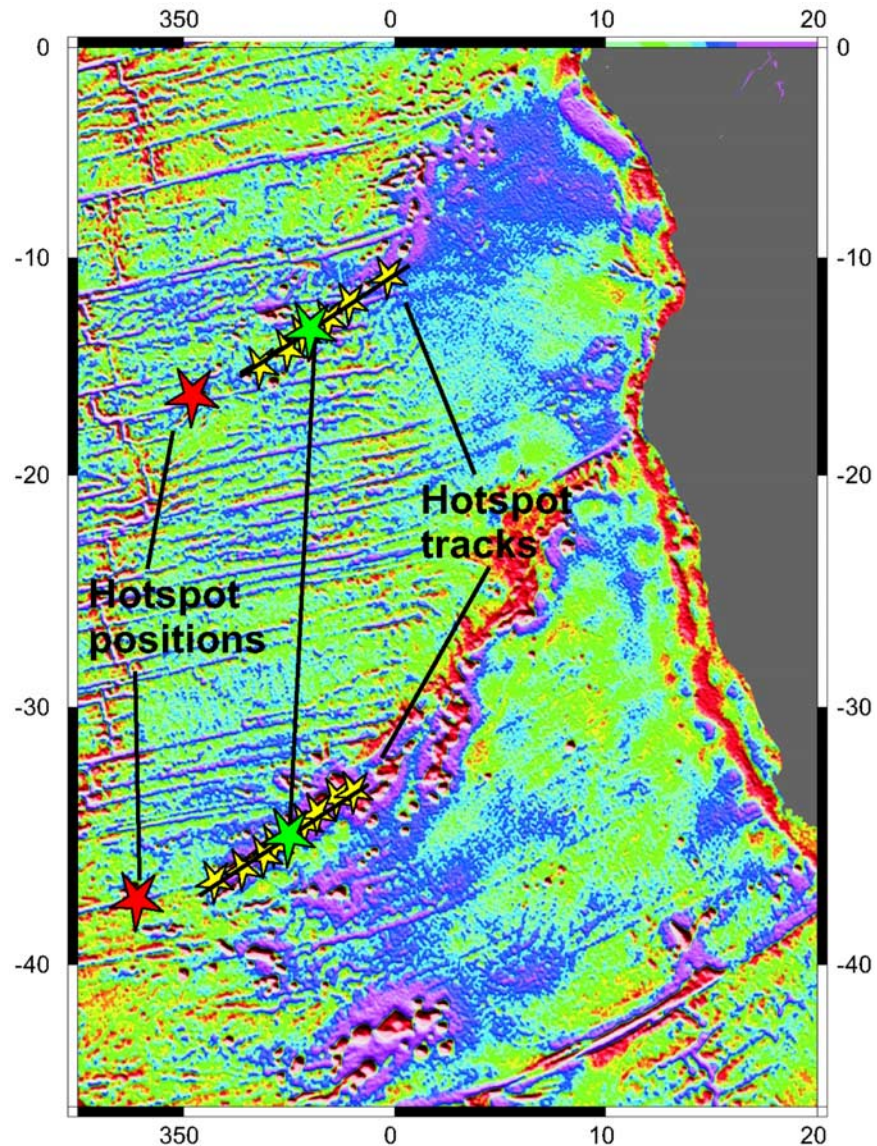
Figure 2. A modified Hellinger criterion of fit for hot spot track reconstructions. Red stars indicates the position of the hot spots, the digitized section of track within the uncertainties of the age we are interested in are shown as yellow stars, and best estimates of the position on the track of the age we want is shown as a green star. The track sections and age positions are considered conjugate data sets (hence we have three sections here, black lines), and they are both reconstructed to the present position of the hot spot.

Providing the reversal sequence has been identified correctly, the main sources of error are locations, and the dates assigned by the reversal timescale.

[13] However, there are important differences between data constraining the history of seafloor spreading and hot spot tracks (Figure 2). One problem with hot spot tracks is the relatively sparse temporal coverage of these tracks [e.g., *Wessel and Kroenke*, 1997]. As a result the focus of hot spot–based reconstructions has been the fitting of hot spot tracks to present inferred positions of these

respective hot spots. These tracks essentially represent the flow lines of the plates relative to the position of the hot spots at the time of their formation. One the other hand, the dating of many hot spot tracks has reached a degree whereby the coverage rivals that of the magnetic anomaly sequence for some areas and times. The problem is that the dated tracks are not uniformly sampled; it is impossible to construct isochrons in the literal sense from sampled hot spot tracks. However, the age uncertainties can be considered along-track, based on the additional constraint that the tracks

represent the flow lines. Conversely, assuming the profile normal to the hot spot track is made uniformly, we can say that the uncertainty in the position of the hot spot when it created a particular section is related to the geometry of the track cross section.

[14] This provides us with two orthogonal data sets (Figure 2). We have dated portions of hot spot tracks u_{ij}; (green stars in Figure 4, i is the segment, j the point (j = 1,.,m_i), and m_i the number of isochron points on the ith segment; in our case, 2). While the uncertainties for given "isochrons" between tracks are likely to be extremely large, it is still possible to estimate the section of a track corresponding to a given time. We also have the track geometry itself (yellow stars in Figure 2), which represents the flow lines of plate motion relative to the underlying mantle, represented by the points v_{ik} (k = 1,.,n_i, where n_i is the number of track points on segment i). The track sections are constrained in length, so that the track length considered is less than the converted 'length' of the along-track timing uncertainties. The best fit rotation will be one which minimizes the misfit of these data sets, and the present (or calculated) position of the hot spots responsible for them. The isochron segments are composed of data from two tracks, which must be fit to the two associated hot spot positions, while the track geometry data set is uniquely fit to its associated hot spot. Thus we have all the ingredients to estimate a rotation for a given time using the Hellinger criterion, which in modified form finds the rotation that minimizes

$$r(A, \eta) = \left(\sum_{i,j=1,2} \overset{\text{Hotspots}}{\left(\frac{h_{i,j}^t \eta_i}{\sigma_{i,j}} \right)^2} + \sum_{i,j=1,2} \overset{\text{Isochrons}}{\left(\frac{u_{i,j}^t A \ \eta_i}{\sigma_{i,j}} \right)^2} \right)$$
$$+ \left(\sum_k \overset{\text{Hotspot}}{\left(\frac{h_k^t \eta_k}{\tilde{\sigma}_k} \right)^2} + \sum_{k,h} \overset{\text{Track geometry}}{\left(\frac{v_{k,h}^t A \eta_k}{\tilde{\sigma}_{k,h}} \right)^2} \right). \quad (1)$$

Here σ and $\tilde{\sigma}$ are the uncertainties in the points interpolated from dated locations, and digitized points along a track section, A is the rotation, and η is the normal to the track section. This assumes the data can be considered to approximate great circle segments. This is obviously not true over the lifetime of a hot spot track; bends in the track, changes in rates of plate motion and, most importantly, hot spot motion all introduce discrepancies into the great circle approximation. However, we argue that since the hot spots we study move around an order of magnitude more slowly

than their overriding plates [see *Raymond et al.*, 2000], the deviations from the great circle approximation for a given interval introduces errors much smaller than the errors inherent in the data. We can also constrain the uncertainties in this estimated rotation, as discussed above, providing we estimate the errors in the data correctly.

[15] For brevity, a discussion of the derivation of Chang's covariance matrix, the measure of uncertainty for a rotation using a Hellinger-style minimization, has been left for Appendix A. Conceptually, the covariance matrix can be thought as describing three small, perturbing rotations that degrade the fit of the data past a certain confidence limit. This is similar to the partial uncertainty rotations of *Molnar and Stock* [1985], and the relationship between these two, together with a discussion of the uncertainties of reconstructed points, can be found in Appendix A.

2.2. Sources of Uncertainty in Hot Spot Reconstructions

[16] Hot spot reconstructions involve finding the best fitting rotation that reconstructs volcanic chains to the present assumed position (or calculated past position) of the hot spot which formed them, for two or more hot spots. Thus one can envisage two sources of error in such reconstructions: uncertainties of the reconstructed sections of volcanic chains (both timing and positional; Figure 3) and uncertainties in the present-day or calculated past positions of the hot spots themselves.

[17] In some cases, current volcanism has been used to infer the present-day position of a hot spot. For example, current volcanism on Reunion Island has been inferred to represent the present surface expression of the Reunion plume [e.g., *Müller et al.*, 1993]. There are a number of possible departures from this simple plume-volcanism relationship that affect on our ability to constrain the position of mantle plumes. First is that melt produced by a plume may be advected laterally, either by asthenospheric conduits [*Morgan*, 1978; *Müller et al.*, 1998] to active ridges, or by sublithospheric topography [*Ebinger and Sleep*, 1998]. This leads to the conclusion that volcanism can occur far from the actual position of a plume, and that plumes can be responsible for volcanism over a wide area.

[18] To give an example, the Walvis Ridge system is widely attributed to a plume located at Tristan de Cunha [*Morgan*, 1971, 1972; *Müller et al.*, 1993]. However, present volcanism occurs on both Tristan
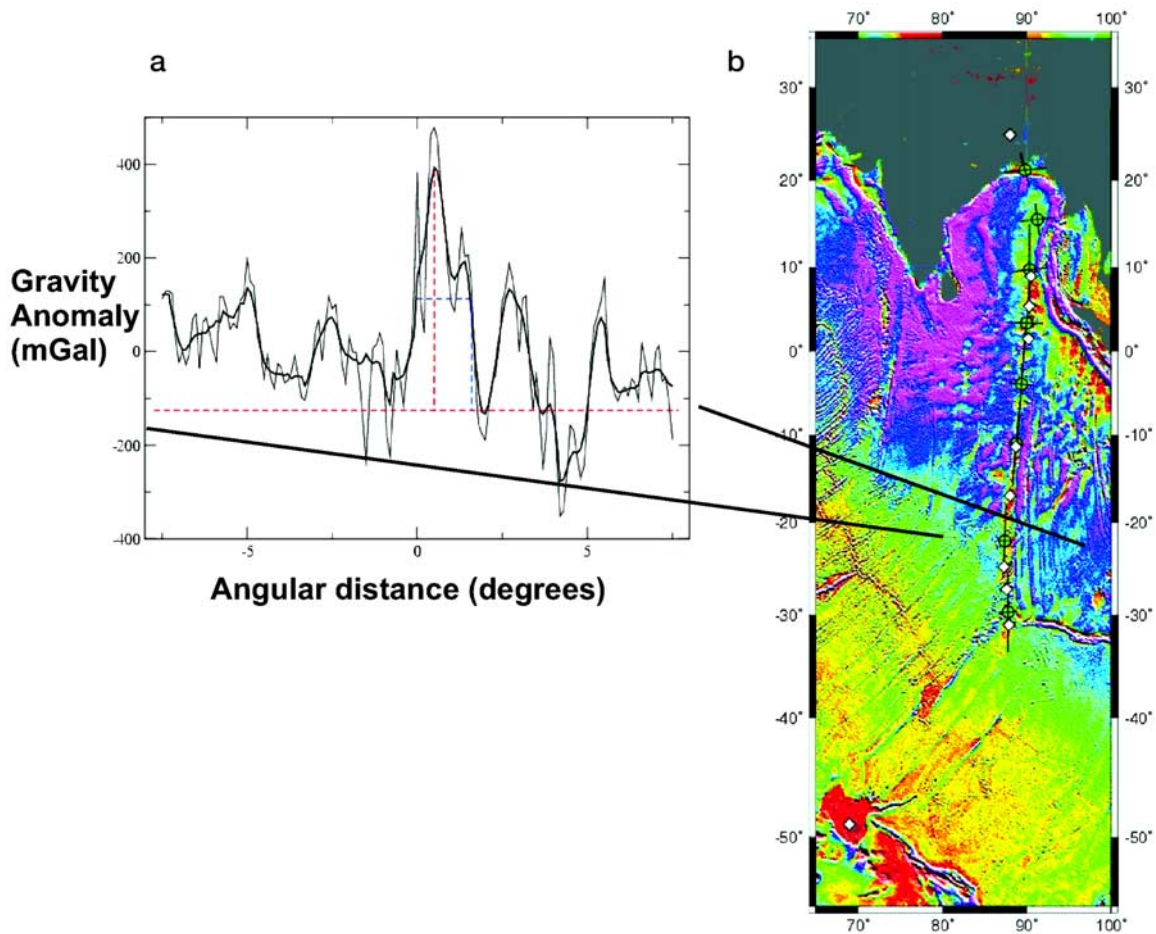
Figure 3. (a) Gravity cross section of the Ninetyeast Ridge, for the segment shown in Figure 3b. The highest point is defined by taking a 1-D filter of the data (thick line) and using a simple neighboring gradient method. The half-width of the profile is defined as the point where the profile crosses the average of the maximum and the average of the lower quartile (assumed base level of the profile). (b) Gravity map of the Ninetyeast Ridge, showing the profile half-widths as defined in Figure 3a, and the along-track errors, which are a combination of radiometric age errors, systematic time errors (see text), and plate velocities, together with their uncertainties, at 10 Myr intervals. The resulting error ellipses are extremely elongate along-track.

de Cunha and Gough Islands [*O'Connor and le Roex*, 1992], and both systems have left distinct lineations within Walvis Ridge, each with its own distinct age progression (see Figure 4). Which island better represents the position of the plume is unclear. Furthermore, *O'Connor and le Roex* [1992] suggest that the wide, distributed volcanism of the Tristan de Cunha and St. Helena hot spot systems may be due to the fact that the volcanic centers themselves are more spatially extensive, and more diffuse, than commonly assumed. One possible explanation of this is that plumes are larger than commonly assumed. Until recently we have had no direct estimate of the diameter of plume conduits, only weak constraints based on their buoyancy flux and our inability to image them tomographically. Recently, *Montelli et al.* [2004]

have presented tomographic images of upwelling plumes. Many of these plumes do not, in fact, have resolvable features extending to the lower mantle. Others, for example Kerguelen-Crozet, seem to have a common source in the lower mantle, suggesting that the initial conduit has split, similar to the suggestion of *Coffin et al.* [2002]. The plume conduits themselves appear to be of the order ∼200 km in the upper mantle, suggesting the volcanism we see is only the minor surface expression of what is, in fact, a fairly large mantle structure.

[19] The uncertainty in the position of a hot spot is even greater for past times. Our flow calculations and conduit modeling represent one attempt at constraining these past positions; however, the
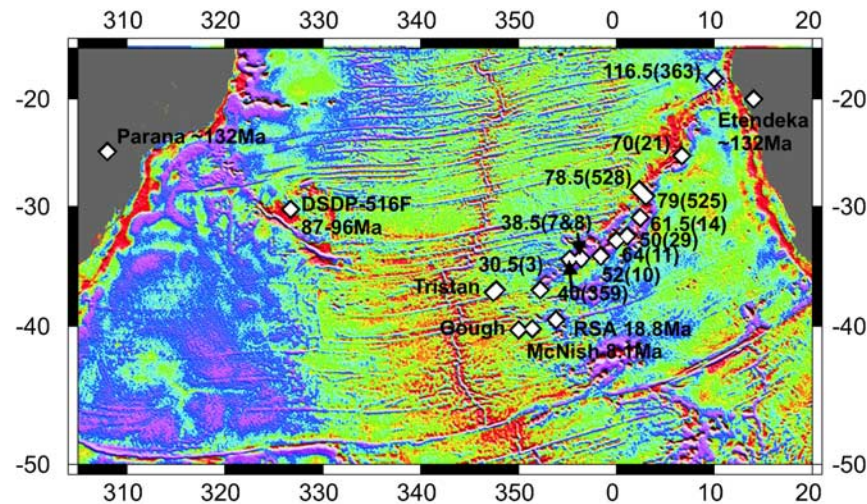
Figure 4. Gravity map of the South Atlantic [*Sandwell and Smith*, 1997] showing the Walvis Ridge and Rio Grande Rise hot spot system. Radiometric ages for the ridge system are shown, as listed in Table 1. Rio Grande Rise and bracketed sample number are from *O'Connor and Duncan* [1990]; Gough lineament data are from *O'Connor and le Roex* [1992]. A variety of sources concur on the age of the Parana and Etendeka volcanics [*Deckart et al.*, 1998; *Morgan*, 1971; *O'Connor and Duncan*, 1990; *Renne et al.*, 1996a, 1996b; *Stewart et al.*, 1996; *Wigand et al.*, 2004].

physical uncertainties in the input to these calculations, together with the uncertainties in modeling assumptions, make it difficult to constrain the uncertainties in these calculated positions in any meaningful way. One possibility is to address the variance in the past hot spot position, for all possible tomography models and all plausible input parameters. This represents an ambitious modeling suite, and is outside the scope of this paper. In addition, the largest discrepancies in calculated hot spot motion are between different tomography models, and we feel some discrimination is required against tomography models that produce unrealistic flow fields and conduit motion. More generally, we should rather only consider those mantle flow models that give a reasonable fit to geoid and other observation, and only collect those results of hot spot motion that are in accord with observations, and the spread of these model results would then be a representation of modeling uncertainties. To some degree, these uncertainties are addressed by the various cases considered in this paper, and in previous work [*Steinberger and O'Connell*, 2000; *Steinberger*, 2000, 2002; *Antretter et al.*, 2002]. Generally, it is found that directions of hot spot motions can be predicted more reliably than its magnitude, and that uncertainty of computed hot spot motion is probably not much smaller than the computed hot spot motion itself. In any case, the uncertainties in our modeling reduce to only one factor in our plate reconstructions: the uncertainty in the past hot spot position.

This is a minimum for the assumed present-day position, and increases in the past. Generally our uncertainty region for our calculated past hot spot position overlaps its present-day uncertainty region.

[20] The uncertainties in reconstructing a volcanic chain can be divided into two groups: those related to the positional uncertainty of a hot spot at the time it created a specific portion of a ridge, and those related to the age of that section. To use the Hellinger criterion we require all the uncertainties in a spatial context, so we translate the age uncertainties into spatial uncertainties by combining them with the estimated angular velocities of the plates (and their uncertainties). Here we make the assumption that the age uncertainties are larger than the inherent spatial uncertainties. This means that we constrain the positional errors by examining profiles across the hot spot chain, and assume timing uncertainties, when converted to spatial uncertainties, fall along-track. The combined uncertainties for a given data point thus form an error ellipse centered on that point, and elongate along the direction of the volcanic chain.

[21] Figure 3 shows a gravity anomaly profile [*Sandwell and Smith*, 1997] across the Ninetyeast Ridge. This profile possesses a degree of uncertainty, in that we have inherent positional uncertainties of the satellite recording the data, and whatever geometric distortions are introduced by the gridding of the data. The highest peak of the

Table 1. Radiometric Ages, Evaluations, and Positions of Sample Points Along Indo-Atlantic Hot Spot Tracks

Sample	Age	±	Comments[a]	λ	θ	Source[b]
			Tristan - Walvis Ridge (Total Fusion Ages)			
AII-93-3-1	30.3	0.3	Concordant,dredge	−37°05.7′	−7°46.7′	1
AII-93-3-25	29.5	0.4	Same site, concordant	−37°05.7′	−7°46.7′	1
AII-93-5-3	38.2	1.1	Isochron age (cc, but not w fusion age)	−34°17.3′	−5°01.5′	1
AII-93-7-1	38.0	0.2	Slightly dc, taken isochron age	−34°30.1′	−3°37.6′	1
AII-93-8-11	37.5	3.5	Slightly dc,total fusion age,same site	−34°29.9′	−3°28.7′	1
AII-93-10-11	52.0	0.3	Unreliable, low argon, min age,dc	−34°20.1′	−1°34.4′	1
AII-93-11-8	64.4	0.4	Slightly dc, tot fusion age	−32°58.2′	−0°01.1′	1
V29-9-1	50.0	0.4	low Ar, dc, plateau age	−32°38.0′	1°07.0′	1
AII-93-14-19	63.4	0.5	cc, tot fusion	−31°59.6′	2°23.6′	1
AII-93-14-1	61.6	0.3	cc, tot fusion, same dredge aa	−31°59.6′	2°23.6′	1
DSDP-525A-57-5,104-106	79.4	0.4	Rock chips combined, slightly dc	−29°04.2′	2°59.1′	1
DSDP-525A-57-6,41-43	79.1	0.4	Tot fusion age, constrained by biostrat and mag	−29°04.2′	2°59.1′	1
DSDP-528-40-5,73-75	79.1	6.3	Isochron age, dc, older than seds or magstrat	−28°31.5′	2°19.4′	1
DSDP-528-41-2,40-42	*62.5*	*0.3*	*dc,arched release pattern, ^{40}Ar loss, younger than seds*	*−28°31.5′*	*2°19.4′*	*1*
Gough lineament						
AG51-2-1 (Tristan)	0.64	0.3	dc plateau & isochron, adopt iso	−37°15′	−12°30′	2
AG51-3-6 (Gough)	0.58	0.07	no iso, used plateau, low Ar	−40°15′	−10°00′	2
AG51-7-1 (McNish)	8.1	0.9	cc, adopt iso	−40°10′	−8°33′	2
AG51-9-1 (RSA)	18.8	0.1	cc. plateau	−39°28′	6°13′	2
Etendeka						
Horingbai dolerite dyke	125	5	see text	~−20°	~16°	3
Tristan - Rio Grande Rise						
DSDP 516F-128-1,22-24	87.2	8.9	Iso age, no plateau age	−30°16.6′	−35°17.1′	1
DSDP-516F-128-1,104-107	95.5	0.5	Extreme inverse staircase release pattern, Total fusion age -dubious, biostrat 84–88Ma.	−30°16.6′	−35°17.1′	1
DSDP-21	74.7–84	?	Biostrat, no basement	−28°26′	−31°18′	1
Parana						
Peak volcanism	125	5	see text	~−26°	~−54°	4
			St. Helena			
Josephine	2.6	0.3	Mean age, single dredge,cc	−16°23.0′	−9°00.7′	5
Benjamine	7.5	0.5	" cc	−16°11.9′	−8°31.0′	5
Kutzov	10.3	0.3	cc	−15°08.4′	−8°21.1′	5
Bonaparte	15.05	0.03	cc, weighted average	−15°48.4′	−6°57.2′	5*
Bagration-shallow	18.8	0.2	cc, weighted av	−15°25.3′	−6°28.5′	5*
Bagration-deep	17.9	0.3	"	−15°22.8′	−6°33.6′	5
St Helena	>7		multiple episodes, most recent age	−17°00.0′	−6°20.0′	5,18
AC-D-06	52.3	0.3	cc, plateau age	−8°25.1′	1°33.0′	2
AC-D-5A	77.6	0.6	cc, isochron age	−4°17.1′	4°28.1′	2
AC-D-2B	81.6	0.4	cc, plateau age(typo W in table?)	−2°19.1′	4°46.1′	2
			New England - Great Meteor			
Monteregian Hills	124.4	1.2	Gilbert & Foland, 86, biotite cc Ar/Ar	~45°	~−73°	6
White Mountains	122.5	1.5	Hubacher and Foland 91, Ar-Ar	~43°30′	~−72°	15
Bear seamount	103.3	2.2	iso age, cc	39°49′	−67°26′	7
Atlantis II seamount	95.4	0.9	dc, recalc total fusion age	38°25′	−63°15′	7
Gosnold	90.8	0.8	cc (not fusion), plateau	38°05′	−62°12′	7
Nashville	81.5	1.2	isochron age	35°18′	−57°33′	7
			Reunion			
Reunion	0.0	2.0	ongoing volcanism, oldest 2 Ma.	−22°00.0	56°00.0	8,11
Mauritius	7.5	7.5	3 phases, 7–8 Ma, 2–3.5 Ma & 0.2–0.7 Ma	−21°00.0″	57°30.0	8,11
Industry well NB-1	31.5	0.5	weighted mean isochron, digitized position	−16°00.0′	60°30.0′	8,17
ODP site 706	32.9	0.7	mean isochron, cc ODP 115	−13°06.8′	61°22.3′	8,9
Industry well SM-1	47.5	3.6	Digitized position	−9°00.0′	59°00.0′	8,17
ODP site 707	64.1	1.1	mean isochron, cc	−07°32.7′	59°01.0′	8,9
ODP site 713	49.6	0.6	"	−04°11.7′	73°23.7′	8,9
ODP site 715	57.5	2.5	"	05°04.9′	73°49.9′	8,9
Deccan	65.5		Hofmann et al.	20°00.0	76°00.0	10

Table 1. (continued)

Sample	Age	±	Comments[a]	λ	θ	Source[b]
			Kerguelen			
			Kerguelen Plateau (recent)			
Heard & McDonald Islands	0.0		Historic volcanism	−53°06.0	72°31.0′	20
Kerguelen	24−30		Younger dikes (0.1−2 Ma, Mt. Ross)	−49°00.0	69°00.0′	19,20
ODP site 1140	34.4	0.6	Duncan (2002) & Weis G3. ODP 183	−46°16.6′	68°29.5′	12
			Ninetyeast Ridge			
DSDP site 254	37.8	1.3	total fusion, cc	−30°58.2′	87°53.7′	22
DSDP site 253	*>44*		*total fusion younger than seds*	−24°52.7′	87°22.0′	22
ODP site 756-D	43.2	0.5	cc, mean plateau age (no pos),ODP121	−26°21.3′	87°35.8′	13
ODP site757	57.9	1.6	slightly dc (no pos). ODP 121	−17°01.4′	88°10.9′	13
DSDP site 214	60.9	1.3	isochron, cc	−11°20.3′	88°43.1′	22
DSDP site 216	*>65*		*sed age, tot fusion unreliable, <81Ma*	*1°27.7′*	*90°12.5′*	22
ODP site 758-A	81.8	2.6	cc, weighted mean site age. ODP 121	5°23.0′	90°21.7′	13
Rajmahal Traps	118.2	0.3		∼24°N	∼88°E	14

[a] Comments are intended as a guide to reliability based on the discussion of the age determinations in the references provided. See references for detailed discussion. Abbreviations used are cc, concordant; dc, discordant; iso, isochron. Italics represent data that were not included in our work, but are included here for completeness.

[b] References: 1, *O'Connor and Duncan* [1990]; 2, *O'Connor and le Roex* [1992]; 3, *Renne et al.* [1996b]; 4, *Deckart et al.* [1998]; 5, *O'Connor et al.* [1999] (*representative positions for combined dredge ages taken from SO84 73DS-1 (shallow) and SO84 71DS-6 (deep)); 6, *Gilbert and Foland* [1986]; 7, *Duncan* [1984]; 8, *Duncan and Hargraves* [1990]; 9, *Vandamme and Courtillot* [1990]; 10, *Hoffmann et al.* [2000]; 11, *McDougall* [1971]; 12, *Duncan* [2002]; 13, *Duncan* [1991]; 14, *Coffin et al.* [2002]; 15, *Hubacher and Foland* [1991]; 16, *Rundle et al.* [1974]; 17, *Meyerhoff and Kamen-Kaye* [1981]; 18, *Chaffey et al.* [1989]; 19, *Nicolaysen et al.* [2000]; 20, *Weis et al.* [2002]; 21, *Morgan* [1971]; 22, *Duncan* [1978].

ridge is assumed to represent the position of the plume at the time it formed this section. To find this we perform a one-dimensional low-pass filter of the data, and use a simple gradient algorithm to find the highest peak. For noncontinuous volcanic chains (e.g., seamount chains) this approach requires manual editing. To estimate the uncertainties in this position we use the half-width of the profile. This is defined by the intersection of the profile with a point halfway between its maximum height, and average background value (mean of the lower quartile).

[22] The uncertainties of the ages of hot spot tracks stem first from the inherent uncertainties in radiometric ages. Given the great expense in obtaining oceanic samples, often the quality of such samples is of small consequence in obtaining an age for them. Techniques in radiometrically dating have obviously improved since the analysis of many of the samples listed here (Table 1). While much of the data are problematic [*Baksi*, 1999], our view is that most are useful, provided we estimate the observational uncertainties correctly. Indeed, the uncertainties in radiometric age are probably minor considering the systematic uncertainties in assigning an age to a particular portion of a volcanic chain.

[23] As an example, we consider the difference in age between the original base of a seamount, and

its most recent volcanic activity. *O'Connor et al.* [1999] give as an example St. Helena Island, where the most recent volcanic activity has been dated at ∼7 Ma. However, on the basis of the age progression of local seamounts, they suggest the base of the island formed around ∼20 Ma. A more extreme example is Kerguelen Plateau. The oldest volcanic activity dates from 118−119 Ma [*Duncan*, 2002], yet ongoing volcanism occurs today at Heard and McDonald Islands. We suggest that for tracks on moderately slow plates, ongoing localized volcanic chain volcanism for ∼15 Myr is plausible.

[24] A related observation is the existence of time reversals on some better-dated hot spot tracks. Two examples include Ninetyeast Ridge and the Walvis Ridge (see Figures 4 and 8). These reversals are probably related to the factors mentioned above, i.e., uncertainties in the ages themselves, ongoing volcanism in different regions at the same time, diffuse volcanic centers possibly related to large diameter plume conduits, and sampling bias between dredge samples (latest, superficial lava flow) and drill sites that reach deeper into basement. Another possibility is that a chain represents the superposed records of two distinct persistent volcanic centers, as may be the case for Tristan de Cunha and Gough. These factors introduce timing uncertainties of at least 10 Myr for the Walvis Ridge, more probably ∼15 Myr. These systematic timing uncertainties are far larger than the assumed

uncertainties in the radiometric ages themselves, and we combine them as percentage errors.

[25] A somewhat more serious point from a statistical point of view is due to the uneven sampling of volcanic chains, and our inability to construct "isochrons" in the standard sense. This led *Wessel and Kroenke* [1997] to introduce a method dubbed "hot spotting" whereby the geometry of hot spot tracks was fit without reference to the age, and with flexibility given to the present position of the hot spot. This methodology alleviates the problems associated with poorly dated hot spot tracks (i.e., it produces a rotation; the time this rotation represents is unspecified). However, it rests on one assumption; the fixity of the hot spots they fit. Given the overwhelming evidence that this does not hold true [*Antretter et al.*, 2002; *Molnar and Stock*, 1987; *O'Neill et al.*, 2003; *Steinberger*, 2000, 2002; *Steinberger and O'Connell*, 1998, 2000; *Tarduno and Cottrell*, 1997; *Tarduno and Gee*, 1995; *Van Fossen and Kent*, 1992], we suggest that absolute plate rotations are somewhat abstract unless we can assign a time interval to them. In our case, we assume a linear rate of spreading between dated points on hot spot tracks, to construct points for the times we are interested in. These points inherit uncertainties from the dates of the locations they are constrained from, and from the assumption of spreading rate. We include these sources of uncertainty in our final analysis.

[26] Finally, we must convert these age uncertainties into spatial uncertainties for use with Hellinger's criterion of fit. This involves combining the time error with the plate's angular velocity for that time, generally obtained from previous fixed hot spot reconstructions. This angular velocity has its own inherent uncertainty, and this must also be considered, and so the spatial uncertainty becomes

$$\Delta \mathbf{d} = \Delta t \Omega + \Delta t \Delta \Omega. \qquad (2)$$

The error ellipses for example points along the Ninetyeast Ridge, at 10 Myr intervals, are shown in Figure 3. The elongate axis reflects the large time uncertainties of each point, expressed along the trend of the volcanic chain. In the following sections we examine five major hot spot chains; the Tristan de Cunha, St. Helena, Great Meteor, Reunion and Kerguelen systems. The tracks are all characterized by their good temporal coverage (at least, for the times that are used) and give us relatively continuous record of hot spot volcanism up to 120 Ma. We review their age progressions, and assess the times for which each track is useful

in our analysis, and assess the evidence for hot spot motion recorded in their paleolatitudes.

3. Hot Spot Tracks

3.1. Tristan de Cunha

[27] Active volcanism today occurs on both Tristan da Cunha and Gough Islands, both widely spaced end-members of the Walvis Ridge volcanic system [*O'Connor and le Roex*, 1992] (Figure 4). The Tristan da Cunha–Gough volcanic system generated the Walvis Ridge on the African plate, and its South American conjugate, the Rio Grande Rise [*O'Connor and Duncan*, 1990; *O'Connor and le Roex*, 1992]. Extensive flood basalts occur on both continental margins, the Parana in South America, and Etendeka on Africa. It has been suggested that these represent the arrival of the original plume head between 129 and 133 Ma [*Morgan*, 1971; *O'Connor and Duncan*, 1990; *Renne et al.*, 1996a, 1996b; *Stewart et al.*, 1996; *Deckart et al.*, 1998; *Wigand et al.*, 2004].

[28] *O'Connor and le Roex* [1992] present ages for samples from Tristan da Cunha and Gough Islands (Table 1). Additionally, *O'Connor and Duncan* [1990] present age data from the Walvis Ridge and Rio Grande Rise, from both dredge samples and DSDP core samples. The data are of varying quality, and we present it in Table 1 with comments on the concordancy of the plateau and isochron ages, which age we adopt in this study, and any additional points of interest on the accuracy of this data. In all a convincing age progression exists for the Walvis Ridge, despite some age reversals which may be due to poor radiometric dates, long-lived localized volcanism, the possibility of two volcanic centers (Tristan da Cunha and Gough), or that the Tristan-Gough system represents a broad zone of more diffuse volcanism [*O'Connor and Duncan*, 1990; *O'Connor and le Roex*, 1992]. The Walvis Ridge is continuous up to the Etendeka Flood Basalts on the Namibian Coast [*O'Connor and Duncan*, 1990]. Unfortunately, the Rio Grande Rise is much more poorly sampled; we present only two radiometric ages, both of dubious quality, from DSDP hole 516 [*O'Connor and le Roex*, 1992]. DSDP 21 also drilled the rise, but did not hit basement. The Rio Grande Rise extends to the Parana Flood Basalts in South America. The duration of magmatism seems to have been about 10–12 Myr [*Stewart et al.*, 1996], the peak volcanism is around 131–133 Ma, consistent with the age of the Etendeka volcanics. Given the two
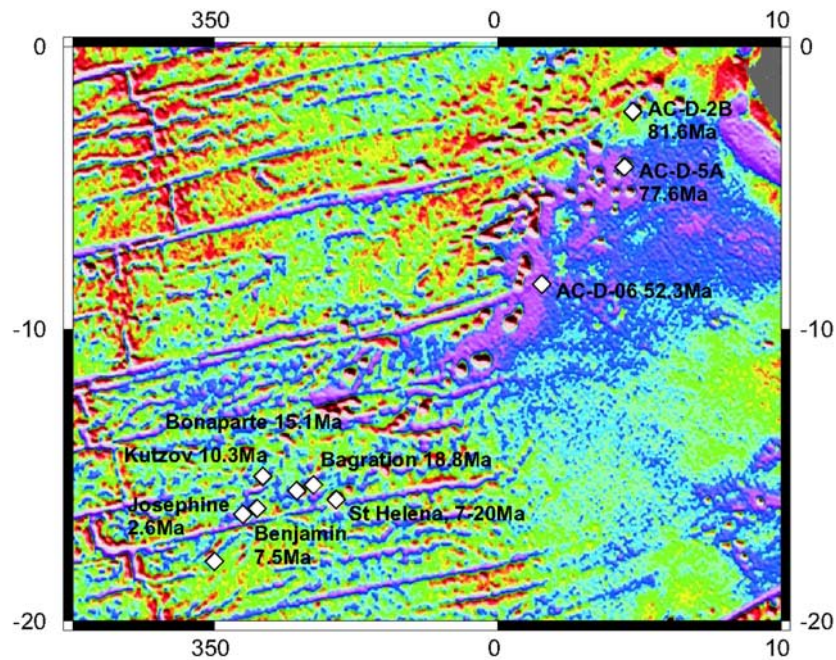
Figure 5. Gravity map [from *Sandwell and Smith*, 1997] of the St. Helena hot spot system. AC-series radiometric dates are from *O'Connor and le Roex* [1992]; all other dates are from *O'Connor et al.* [1999].

distinct age progressions of the Tristan da Cunha and Gough lineaments, we use ages only from the northernmost lineament, and take Tristan da Cunha as the current position of the hot spot. Where time-reversals exist (i.e., a nonlinear progression of ages), we use the oldest reliable ages reported.

3.2. St. Helena

[29] *O'Connor and le Roex* [1992] present age data for the St. Helena seamount chain, and demonstrate a clear age progression. However, this progression did not continue to the Cameroon volcanics in west Africa; indeed any record of activity of St. Helena near the African coast appears to have been covered by more recent volcanic activity [*O'Connor and le Roex*, 1992]. *O'Connor et al.* [1999] dated the younger part of the St. Helena chain, mostly the seamounts to the west of St. Helena Island itself. They found the youngest evidence for volcanism at the Josephine seamount (2.6 Ma; see Figure 5), with ages increasing to the east toward St. Helena. Indeed, the seamount nearest St. Helena, Bagration, they found to be 18.8 Ma. While their data seem to suggest an age for St. Helena Island of ∼7 Ma, based on the apparent age progression they suggest volcanism started on St. Helena at around ∼20 Ma. While the St. Helena seamount chain does not fit the classic, consistent volcanic chain model, the ages sampled help fill in the volcanic record for Indo-Atlantic hot spots in the 0–30 Ma window,

which in previous models was constrained only by Reunion. We take the Josephine seamount as the current position of the St. Helena plume, and use it in reconstructions for ages less than 82 Ma.

3.3. Great Meteor

[30] The Great Meteor–New England seamount chain (Figure 6) is one of the oldest chains used in our analysis; the Monteregian Hills volcanics, which represent the earliest reliable evidence of the hot spot, are around 124.4 Ma [*Gilbert and Foland*, 1986]. Some controversy exists as to the current volcanic center [*Duncan and Richards*, 1991; *Müller et al.*, 1993; *O'Connor and Duncan*, 1990; *Tucholke and Smoot*, 1990]. Here we adopt Seamount 18 of the Great Meteor group, after *Müller et al.* [1993] and *Tucholke and Smoot* [1990]. An apparent age progression, inferred from the subsidence of the seamounts, exists, trending to Seamount 18 [*Tucholke and Smoot*, 1990]. This seamount is also peaked, which suggests it is younger than the more northern flat-topped seamounts in the group.

[31] The Great Meteor hot spot has been inferred to have been responsible for the Cretaceous volcanism in the White Mountains and Monteregian Hills (∼124.4 Ma) [*Gilbert and Foland*, 1986], before forming the New England seamount chain (105–80 Ma) [*Duncan*, 1984] and the Corner
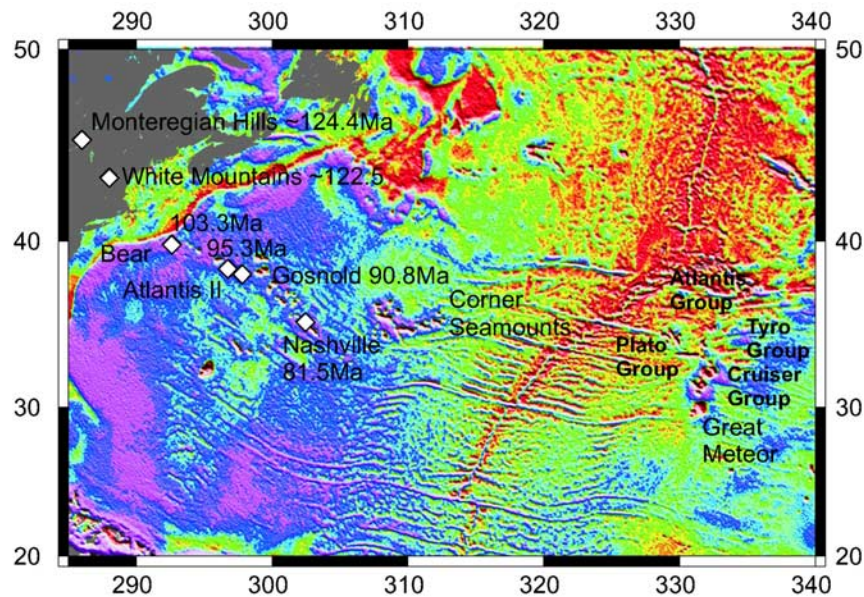
Figure 6. Gravity map [from *Sandwell and Smith*, 1997] of the Great Meteor hot spot system. Radiometric dates for the New England seamounts are from *Duncan* [1984]. An age progression from the New England seamounts to the Corner seamounts and the Great Meteor group has been shown by *Tucholke and Smoot* [1990] on the basis of seamount subsidence curves. Ages for White Mountains and Monteregian Hills are given by *Gilbert and Foland* [1986].

Seamounts (∼75 Ma) [*Tucholke and Smoot*, 1990]. Around this time, the hot spot crossed onto the African plate, where it has subsequently created the Atlantis-Plato-Tyro-Cruiser-Great Meteor seamount groups (0–70 Ma) [*Tucholke and Smoot*, 1990]. Unfortunately, no radiometric ages exist for the track for ages younger than 80 Ma (i.e., its entire history on the African Plate, and the Corner Seamounts). Evidence for age progression was presented by *Tucholke and Smoot* [1990], on the basis of seamount subsidence curves, and these broadly support the above history. Radiometric dates have been presented for the New England part of the chain [*Duncan*, 1984]. These show a consistent age progression from the Nashville seamount in the east, to the Bear seamount to the west, and are presented in Table 1. Due to the lack of dates for younger times, the Great Meteor hot spot is used in our analysis only for ages greater than 80 Ma.

3.4. Reunion

[32] Reunion Island consists of two volcanoes; the inactive Piton des Neiges to the north, and the currently active Piton de la Fournaise in the south [*Duncan*, 1990]. The present position of the Reunion hot spot is commonly taken to be Reunion Island itself, although a large seamount currently 160 km west of Reunion may represent the most recent activity of the hot spot [*Duncan*, 1990].

[33] It is widely supposed that the arrival of the Reunion plume head beneath India was responsible for the Deccan flood basalts at 65.5 Ma [*Courtillot et al.*, 1986; *Duncan and Pyle*, 1988; *Hofmann et al.*, 2000]. The arrival of the Reunion plume has been suggested to be responsible for the separation of the Seychelles microcontinent at this time [*Gaina et al.*, 2003]. Subsequent to this, it formed the Laccadives-Maldives-Chagos ridge on the Indian plate (Figure 7), and its African conjugate the Mascarene Plateau–Nazareth Bank–Mascarene Islands group [*Duncan and Hargraves*, 1990]. Two industry wells (SM-1 and NB-1) were drilled by Texaco in 1975 on the Saya de Malha Bank and Nazareth Bank, respectively [*Duncan and Hargraves*, 1990; *Meyerhoff and Kamen-Kaye*, 1981]. DSDP Leg 115 also drilled the two ridge systems, and recovered basement from four drill sites [*Duncan and Hargraves*, 1990]. As a result, good age progressions exist of both of these ridge systems (see Table 1), and support a Reunion hot spot origin for these features [*Duncan*, 1990].

[34] The Mascarene Islands group commonly refers to the islands of Reunion, Mauritius and Rodrigues. Earliest volcanism at Mauritius appears to have been around 7–8 Ma [*Duncan and Hargraves*, 1990]. Two subsequent phases of volcanism (at 2–3.5 and 0.2–0.7 Ma) have been ascribed to the long thermal response time of the lithosphere
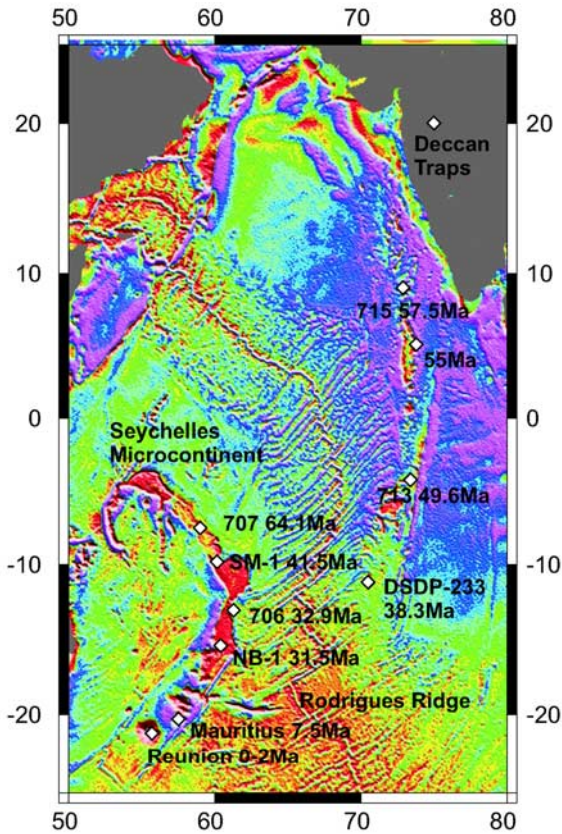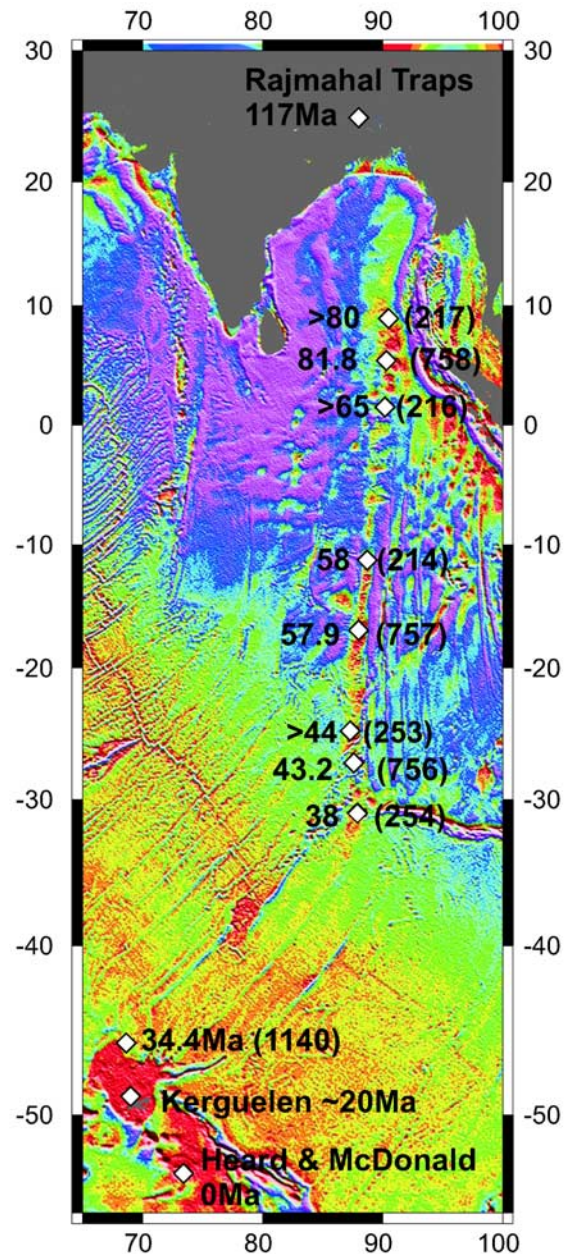
Figure 7. Gravity map of the Reunion hot spot system [from *Sandwell and Smith*, 1997]. Radiometric dates are from *Duncan and Hargraves* [1990] and also *McDougall* [1971] for Mauritius and *Hofmann et al.* [2000] for the Deccan Traps.

[*Duncan and Hargraves*, 1990]. An alternative is the sublithospheric advection of melt; indeed this has been proposed for origin of the Rodrigues Ridge [*Morgan*, 1978]. Rodrigues Island, which is the only subaerial expression of the ridge, lies halfway between Mauritius and the Central Indian spreading ridge, and has been dated at 1.5 Ma [*McDougall*, 1971]. *Morgan* [1978] proposed that the ridge formed due to asthenospheric flow from the hot spot to the nearby spreading ridge. The earliest volcanism at Reunion Island is at 2 Ma [*Duncan and Hargraves*, 1990], and so it is assumed the hot spot was situated beneath the island at this time. Hence the late phases of volcanism at Mauritius, and the formation of the Rodrigues ridge, can both be explained by an asthenospheric flow model.

3.5. Kerguelen

[35] The Kerguelen hot spot has a long and somewhat complicated history (Figure 8). The oldest

volcanics attributed to it are the 123–132 Ma Bunbury basalts in Western Australia [*Frey et al.*, 1996; *Ingle et al.*, 2002; *Storey et al.*, 1992]. Subsequently, it formed the South Kerguelen Plateau (110–119 Ma) [*Coffin et al.*, 2002; *Duncan*, 2002] on the Antarctic plate, and the Rajmahal

Figure 8. Gravity map of the Kerguelen hot spot system [from *Sandwell and Smith*, 1997]. DSDP sites 253 and 254 are from *Rundle et al.* [1974], DSDP sites 214 and 216 are from *McDougall* [1973], ODP sites 756–758 are from *Duncan* [1991], the age progression across the Kerguelen Plateau is documented by *Weis et al.* [2002], and the Rajmahal Traps dates are from *Coffin et al.* [2002].

Traps (117 Ma) [*Coffin et al.*, 2002; *Kent et al.*, 2002] on the Indian Plate. Lamprophyres in northeastern Indian and Antarctica dating around 114–115 Ma have also been attributed to the Kerguelen hot spot [*Coffin et al.*, 2002]. Basalts from Elan Bank suggest this microcontinent separated at this time [*Coffin et al.*, 2002], certainly after 124 Ma as suggested by plate kinematics [*Gaina et al.*, 2003]. Central Kerguelen Plateau, and its conjugate on the Australian plate, Broken Ridge, formed at around 100 Ma and 95 Ma, respectively [*Duncan*, 2002]. The problem with the plume-head model for the extensive volcanism around this time is that plate reconstructions place these features several thousand kilometers apart at this time, requiring a plume head also of this size [*Coffin et al.*, 2002]. However, active spreading had begun by this time between the India-Australia and Antarctica, so the question becomes how does melt erupt on the surrounding continents without any record of it in the young spreading centers separating these continents? *Coffin et al.* [2002] documents the magmatic history of the Kerguelen plume, and suggests either two separate plume sources, or that the Kerguelen plume was split into several diapirs. The latter interpretation has a curious parallel in the recent tomographic imaging of the deep plume structure by *Montelli et al.* [2004]. They propose a common source for the Kerguelen and Crozet plumes, at a point north of Crozet, in the deep lower mantle. This clearly supports a model of shearing of plume conduits into several subconduits, a behavior which has been well-documented in laboratory experiments [*Olson and Singer*, 1985]. Indeed, this is seen in many of the conduits imaged by *Montelli et al.* [2004] in the Atlantic and south Pacific, and seems to be a common occurrence.

[36] For our reconstructions, though, we are interested only in the times for which Kerguelen can be modeled by a single conduit. Thus we restrict ourselves to the history of Kerguelen as it formed the Ninetyeast Ridge, and the Rajmahal Traps (i.e., 37–117 Ma). A good age progression exists for these times (see Table 1). The origin of the Rajmahal Traps has been widely debated. Geodynamic reconstructions, following *Curray and Munasinghe* [1991], suggest that the Crozet hot spot was responsible for the 85-East Ridge and the Rajmahal Traps. However, inconsistent isotope systematics between the Crozet Archipelago, the Afanasy-Nikiti (~80 Ma) seamount, and the Rajmahal Traps argue against this model [*Kent et al.*, 1997]. Reconstructions including moving

hot spots show that a Kerguelen plume ~10° north of its current position is completely consistent with the formation of the Ninetyeast Ridge and Rajmahal Traps [*Antretter et al.*, 2002; *O'Neill et al.*, 2003], and most recent isotopic constraints concur with this interpretation [*Baksi et al.*, 1987; *Kent et al.*, 2002; *Weis et al.*, 2001].

[37] For younger times, the plume has been beneath the northernmost Kerguelen Plateau. Thus a well-constrained track does not exist for Kerguelen for younger times, since the Antarctic plate has been relatively stationary over this period. *Weis et al.* [2002] document an age progression for the plume under the north Kerguelen Plateau, suggesting it has moved south with respect to the Antarctic plate during this time. Kerguelen Island itself appears to have been formed 24–30 Ma [*Nicolaysen et al.*, 1996]. Ongoing volcanism occurs on Heard and McDonald Islands, which suggests the current position of the plume is in this vicinity [*Nicolaysen et al.*, 1996].

4. Results

4.1. Hot Spot Motion Models

[38] Our calculated hot spot motions show a degree of variability, depending on the tomography model, viscosity structure, seismic velocity conversion factor, phase changes, and plume model used.

[39] Figure 9a shows the calculated motion of our selected Indo-Atlantic plumes, for three different tomography models. The Scripps and Harvard S12WM13 models both use seismic velocity to density conversion factors of 0.2, while the Grand-2000 model (downloaded by anonymous ftp, 2000; similar to *Grand et al.* [1997]) is converted to density anomaly based on a conversion factor of 0.35 to account for its lower amplitudes. The same plume model was used for all three cases, where a D″ source was assumed and the ratio of interior to exterior viscosities was held constant at 0.1. The same radial mantle viscosity profile (v35) was assumed for all cases, and a Clayperon slope of −2.5 MPa/K for the spinel-perovskite/magnesiowustite transition at 670 km and 2 MPa/K for the olivine-spinel transition (default value unless otherwise stated). Large variations in plume motion exist between the models. For example, the Scripps model consistently predicts a northward motion of Kerguelen, Tristan da Cunha and Great Meteor plumes. This is at odds with paleomagnetic evidence [*Antretter et al.*, 2002; *Van Fossen and Kent*,
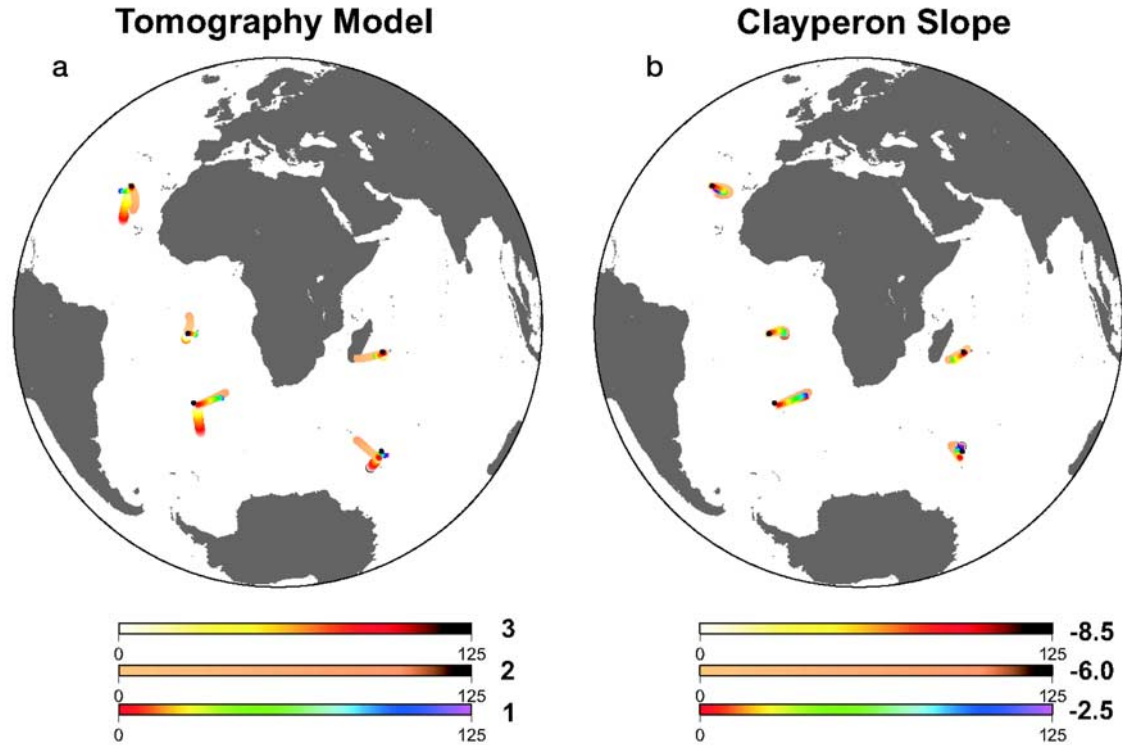
Figure 9. (a) Calculated plume motion for the Scripps [*Masters et al.*, 2000], Grand- 2000, and Harvard s12wm13 [*Su et al.*, 1994] seismic tomography models. Note wider tracks have been plotted for the Scripps and Grand models for visibility. The same plume model and viscosity structure (35) were used for each simulation. Seismic velocity conversion factors of 0.2 were used for the Scripps and Harvard models, while 0.35 was used for the Grand model to account for its lower amplitudes. (b) Hot spot motion for different values of the Clayperon slope (MPa/K) for the spinel-perovskite phase transition at ~670 km. The critical value for layered convection from 2-D simulations is −6 MPa/K [*Christensen and Yuen*, 1985].

1992] and so these models were eliminated early in the selection process. Figure 9b shows the motion of plume conduits for different values of the Clayperon slope (in MPa/K) for the spinel-perovskite phase transition at ~670 km, for the S12WM13 tomography model. Previous two-dimensional simulations found the critical value for layered mantle convection to be −6 MPa/K [*Christensen and Yuen*, 1985]. We varied this parameter past this range, and also experimented with an additional phase change at ~410 km (olivine-spinel, Clayperon slope ~2 MPa/K), but found this had little effect on our calculated hot spot motions. Our preferred values for the Clayperon slope are −2.5 MPa/K for the spinel-perovskite transition and 2 MPa/K for the olivine-spinel transition.

[40] Figure 10b shows the variety of viscosity structures used in our simulation, and Figure 10a shows the calculated hot spot motion for a selection of these profiles. All models use our preferred Clayperon slope parameters, and tomography model

S12Wm13. Viscosity structure 35 is similar to the preferred viscosity model of *Steinberger and O'Connell* [1998]. Viscosity 37 shows an exaggerated jump at the 670 km discontinuity, and viscosity structure 39 is more similar to viscosity profiles determined from geoid modeling [*Forte and Mitrovica*, 1991; *King*, 1995; *King and Masters*, 1992; *Ricard et al.*, 1989], with a milder viscosity contrast at 670 km, and comparatively higher upper mantle viscosities, and lower viscosities in the lower mantle (Figure 10b). While the broad features of the motion of the plumes are similar across all models, the magnitude of this motion varies considerably. The largest amounts of motion are observed for viscosity structure 35, with lesser amounts for 37 and 39, respectively. This is consistent with the observation made by *Steinberger and O'Connell* [1998] that the motion of a conduit is dominated by the overall viscosity contrast between the upper and lower mantle.

[41] Figure 11a shows the results of three different plume models in the same mantle flow field. The
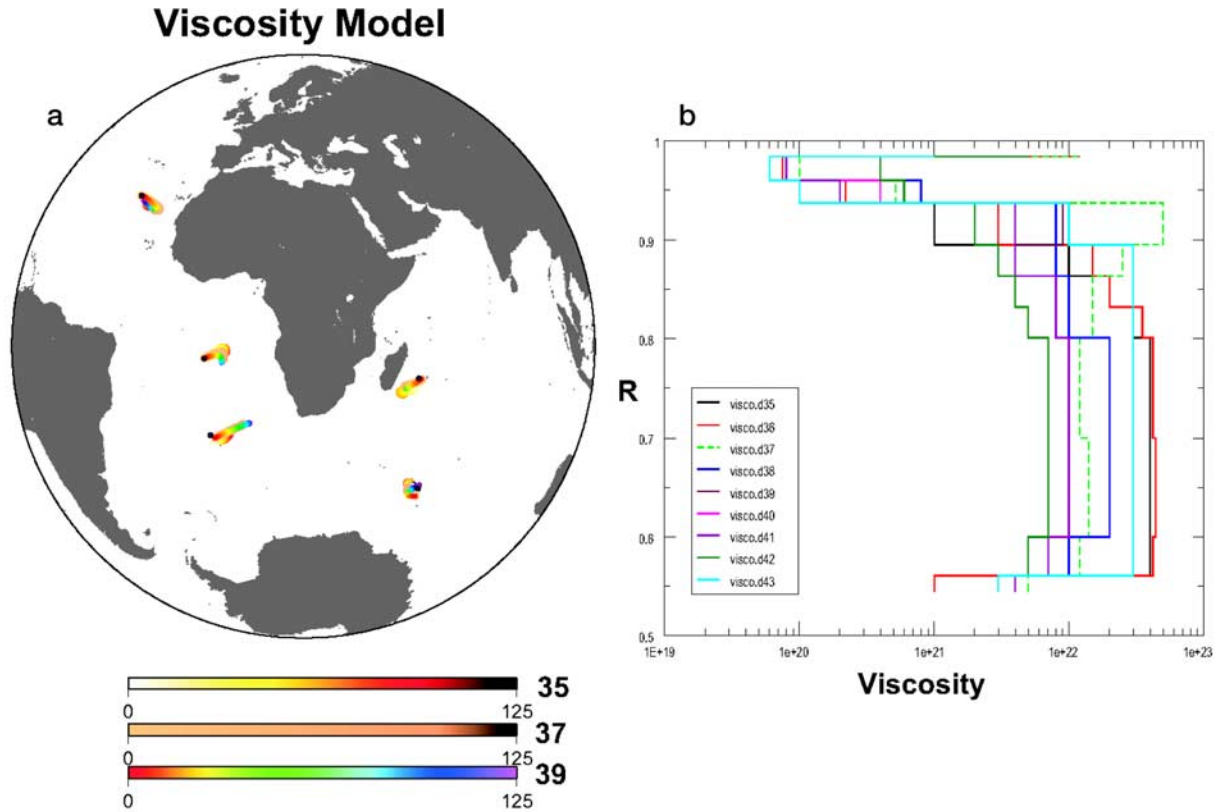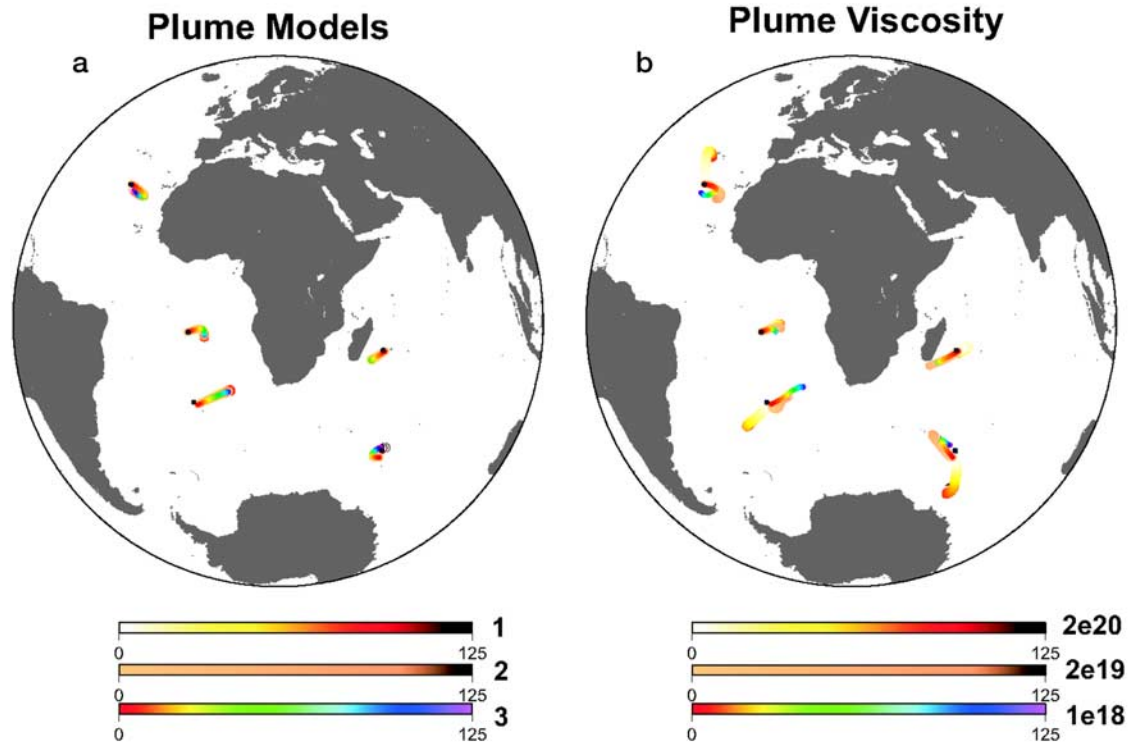
Viscosity Model

Figure 10. (a) Hot spot surface motion for the last 125 Myr for three different viscosity models (35, 37, and 39). Note the track thicknesses vary for visibility. (b) Radial mantle viscosity profiles (Pas) used in the simulations. The range of allowable values is constrained by postglacial rebound and geoid modeling. Our preferred structure differs from *Steinberger and O'Connell* [1998] by having less viscosity contrast between the upper and lower mantle, in line with geoid modeling.

flow field was calculated for the *Su et al.* [1994] model, with a seismic velocity to density conversion factor of 0.18. Viscosity model 42 was used to calculate the flow field. The motion of the plume conduits is a combination of the mantle flow velocity, and the buoyant rising speed of the conduit element u, given by

$$u = \frac{k_c \Delta \rho g}{\eta_{out}} \sqrt{\frac{8B\eta_{in}}{\pi \Delta \rho dp/dz}}. \tag{3}$$

Here $\Delta \rho$ is the density difference between the conduit and the surrounding mantle ($\sim$30 kg/m³ [*Steinberger and O'Connell*, 2000]), g gravity, η_{in} and η_{out} the internal and external viscosities, B the anomalous mass flux, and dp/dz the nonhydrostatic pressure gradient driving the flow (assumed to be $\Delta \rho g$). The value of the parameter k_c was determined by *Richards and Griffiths* [1988] to be 0.54 for chemical plumes. Three different plume viscosity models were used. Plume model 1 has a constant viscosity of 10^{19} Pas within the plume

conduit for all depths. However, temperatures may be assumed adiabatic within the conduit, as well as outside, in which case the ratio of internal to external viscosities may be constant. On the other hand, thermal entrainment may result in an increase in this ratio with depth. With this in mind, plume model 2 has a constant viscosity of 10^{19} Pas beneath the lithosphere, until the external viscosity exceeds 10^{20} Pas. Then the ratio of internal conduit viscosity, and the external viscosity for the previous radial layer, was held constant at 0.1. Plume model 3 is similar, and has a constant viscosity of 1e19 beneath the lithosphere. Where the external viscosity exceeds 10^{20} Pas, however, the ratio of internal conduit to external mantle viscosities (for the same radial layer) was held constant at 0.1. The differences between the models, in this example, lie chiefly in the magnitude of motion predicted. The least motion is predicted for plume model 3, our most realistic plume model. For other less realistic parameter ranges, the differences between the plume models can be extreme.

Figure 11. (a) Hot spot motion for three different plume models. Model 1 has a constant viscosity of 1e19 Pas inside the plume conduit. In model 2 the viscosity of the conduit beneath the lithosphere is assumed to be 1e19 Pas, and the ratio of internal to external viscosity in the previous radial layer is constant. Model 3 is similar to model 2, with the ratio of internal to external viscosity in the same radial layer held constant. Flow field is based on the S12WM13 model, with viscosity structure 42, dv/dp ∼ 0.15, and preferred thermodynamic values (see text). (b) Hot spot motion for different plume internal viscosities, for plume model 3. Internal viscosities listed are for beneath lithosphere, the ratio of internal conduit viscosity to external viscosity (Viscosity model 42) is constant; otherwise as in Figure 11a.

[42] The flow field calculations for Figure 11b are similar to Figure 11a (above), with the viscosity model 42. We also use plume model 3 (as above) for all three cases. The difference between the models is in the ratio of internal to external viscosities. Our motivation for this is that hotter plumes generally have lower internal viscosities [Steinberger, 2000], and this has a discernible difference on hot spot motion. An internal conduit viscosity of 2×10^{20} Pas beneath the lithosphere is probably unrealistic, as this exceeds most viscosity estimates of the asthenosphere [e.g., King, 1995]. This value also results in a fairly large conduit radius, and unrealistic plume motions (e.g., Kerguelen motion is not consistent with paleomagnetic constraints). The other two sublithospheric viscosities (2×10^{19} Pas and 10^{18} Pas) are closer to expected conduit viscosities. While some features of the motion are consistent, the magnitude of the calculated motion, and the positions of the plume through time vary considerably. Depending of the other parameters chosen, this difference in internal plume

viscosities can be one of the most important factors in our motion models. This is an important difference between our plume models and previous studies [Steinberger, 2000], where only smaller variations in internal plume viscosity were considered, as this provides an additional degree of freedom to our plume motion, and allows us to investigate the causes for differences in plume motion within the same mantle flow field model.

[43] Figure 12a shows our preferred hot spot motion model. The model represents a convergence on our preferred parameter ranges over several generations of simulations. The tomography model is the Harvard s12wm13 model. While an older model, and of lower resolution (12th degree spherical harmonic), it does give us consistent and sensible hot spot motions over a range of parameter values. Our preferred viscosity structure is viscosity model 42 (Figure 10b), and our preferred plume model is model 3. The heat transport for each of our hot spots [from Sleep, 1990] is 79GW for
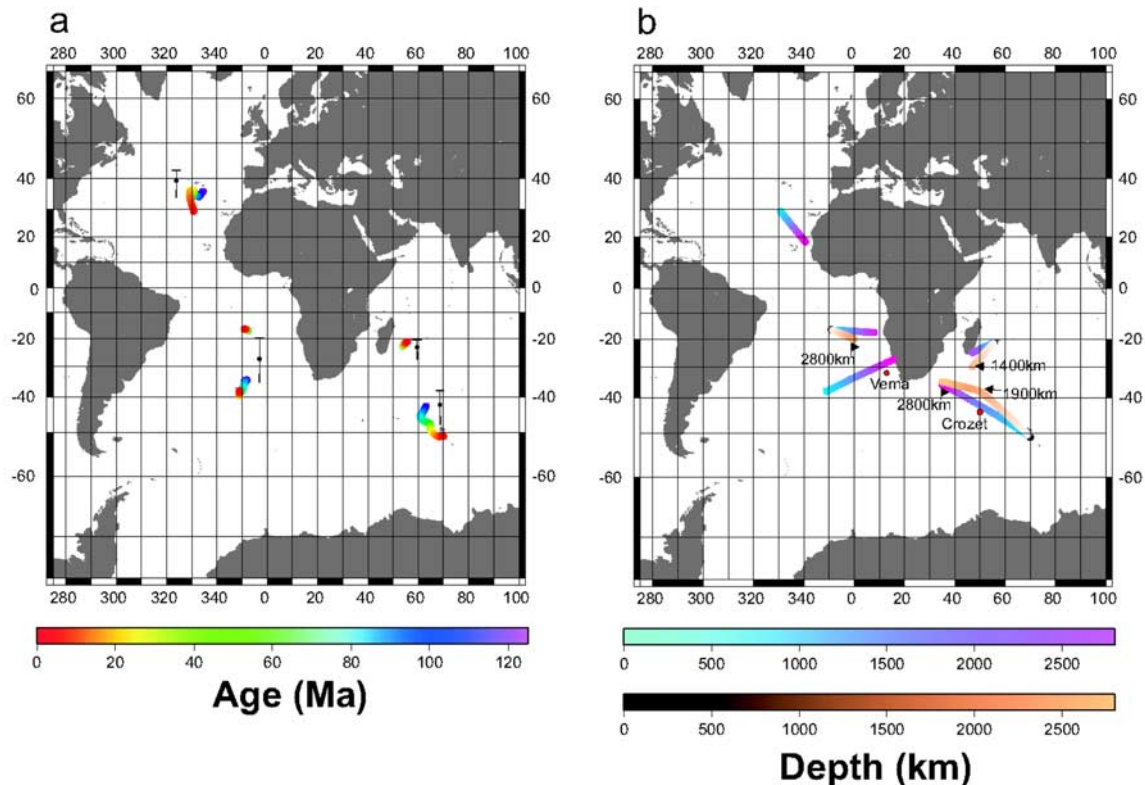
Figure 12. Our preferred hot spot motion model, based on our interactive evolutionary approach, with selection criteria including paleomagnetic and geological constraints, as listed in Table 2. The paleolatitudinal constraints for Great Meteor are from *Van Fossen and Kent* [1992]; those for Tristan are modified from *Van Fossen and Kent* [1992], with uncertainties modified after *Ernesto et al.* [1990]. Reunion paleolatitude estimates are from *Vandamme and Courtillot* [1990], and those for Kerguelen are from *Antretter et al.* [2002]. (b) Modeled conduit tilt (blue-magenta color scale) for our preferred hot spot motion model, shown to 2800 km. Also shown are constraints on conduit tilt from the model of *Montelli et al.* [2004] (copper color scale), interpreted and digitized at 1900 and 2800 km for the Kerguelen/Crozet plume, 2800 km for the St. Helena/Ascension plume, and 1400 km for the Reunion plume. The modeled tilts suggest that the Crozet plume is a later diapir that formed from a strongly tilted Kerguelen plume. The strong tilt of the Tristan da Cunha plume also suggests it may have formed secondary diapirs, of which the Vema seamount may be a surface expression.

Reunion, 71GW for Tristan da Cunha, and 21GW for St. Helena, Great Meteor and Kerguelen. We note that these values are deduced from the cross-sectional area of the swell, and so are subject to uncertainties depending on the position of the hot spot, preexisting structure over the hot spot (as in the case of Kerguelen), and the existence of more than one volcanic center (as is the case for Tristan da Cunha). Nonetheless, we use these as a proxy for plume internal temperatures, and subsequently internal plume viscosities. The justification for this is that while these plumes may start at the same source (D″), weaker plumes will cool faster [*Albers and Christensen*, 1996], and reach the lithosphere with higher viscosities. Since the viscosity at shallower depth should matter more to computed hot spot motion than at large depth, the assumption of a viscosity ratio that is constant with depth, but

different for different plumes appears a reasonable simplification. We use an internal conduit viscosity immediately below the lithosphere of 5×10^{18} Pas for Reunion and Tristan, and 2×10^{19} Pas for Kerguelen, Great Meteor and St. Helena (note this varies with depth, such that the ratio of internal to external viscosities is constant (0.1 for conduit viscosity of 4×10^{19} immediately below the lithosphere).

[44] The selected data shown in Figure 12a are for ages closest to the maximum age of the hot spot chain. The paleolatitudinal evolution of Kerguelen in discussed by *Antretter et al.* [2002] and *O'Neill et al.* [2003]. The Kerguelen plume consistently exhibits a southward motion in dynamic models, in line with paleolatitude constraints. These paleolatitudes cannot be explained by TPW [*Antretter et*

al., 2002]. Our modeled motion of the Reunion plume is consistent with the paleolatitudinal constraints of *Vandamme and Courtillot* [1990]. It is also, however, consistent with paleolatitudes expected from TPW [*O'Neill et al.*, 2003; *Vandamme and Courtillot*, 1990], or a combination of both TPW and hot spot motion [*O'Neill et al.*, 2003]. *Van Fossen and Kent* [1992] present evidence for a southward drift of the Great Meteor and Tristan da Cunha hot spots between 120 and 90 Ma. Their predicted motion for Tristan da Cunha is ~13 degrees. This paleolatitudinal drift is derived from the African APW path, and so is subject to a TPW signature. Also, the Etendeka and Parana flood basalts are quite extensive, and extend over a range of latitudes. We adopt the paleolatitudes of Ernesto [*Ernesto et al.*, 1990], modified to a revised position of the hot spot at this time.

[45] The tilts for these plume motion models are also shown in Figure 12b. The conduits are shown down to their assumed source at D″. The source region in these simulations migrates due to return flow in D″, resulting in greater tilts for these models than for simulations assuming a fixed plume source. We have also interpreted and digitized the present conduit tilts of the St. Helena, Kerguelen and the Reunion plumes from the tomography model of *Montelli et al.* [2004]. The Kerguelen-Crozet plume has been interpreted at 1900 and 2800 km, and has a strong signal down to the lower mantle. The St. Helena-Ascension plume has been interpreted at 2800 km depth. The Reunion plume is not discernible to the lower mantle, though this may be a resolution problem. We have digitized its position at 1400 km from the online supplement of *Montelli et al.* [2004]. The tilt of the plume conduits agree within the limits of resolution of the tomography, and the uncertainties in our conduit models.

4.2. Revised Indo-Atlantic Rotations

[46] Table 2 presents revised finite rotations for the Indo-Atlantic reference frame, using a modified Hellinger criteria of fit for hot spot tracks. The results are for our preferred hot spot motion model. The scaled covariance matrices for each rotation are also shown.

[47] Figure 13 shows the calculated tracks for the best fit rotations of Table 2. The brown lines represent the calculated tracks for fixed hot spot reconstructions, the colored circles are the tracks for our preferred hot spot motion model in Figure 12. The fit of the fixed hot spot tracks to the actual tracks is severely degraded in a number of instances.

In particular, the fit of the New England seamount track for ages between 80 and 120 Ma is poor for fixed hot spots. Similarly, the fit to the Ninetyeast Ridge is extremely poor if one considers a fixed Kerguelen plume. This has been previously noted by *Royer et al.* [1991] and *Müller et al.* [1993]. *Royer et al.* [1991] noted that the fit is improved if the Kerguelen plume was further north between 30 and 90 Ma, in line with paleomagnetic constraints. The model of *Müller et al.* [1993] is shown as red lines in Figure 13. The tracks are calculated using our inferred present-day hot spot positions, shown as blue crosses. The main problem with the fit of *Müller et al.* [1993] model is the fit of the Ninetyeast Ridge. *Müller et al.* [1993] had to assume that the present position of the Kerguelen hot spot was of the west bank of the Kerguelen Plateau, and could not reconcile a fixed Kerguelen hot spot with the position of the Rajmahal Traps. These problems are alleviated for tracks calculated using our preferred motion model.

[48] Also shown in Figure 13 are error ellipses corresponding to the uncertainties in the position of the rotation poles for the listed times, for fixed and moving hot spots. These ellipses represent a projection of a 3-D ellipsoid onto the latitude-longitude surface, and they do not uniquely constrain the rotational uncertainty. To give an example, two rotations with the same pole, but with angles of rotations of, say, 10° and 90°, will generally be statistically different, but will have overlapping pole uncertainty ellipses. The uncertainty regions become smaller with increasing age; this is because smaller rotations are more poorly constrained and have larger uncertainty regions (see Appendix A for discussion). That is, a small deviatoric rotation, added to a small rotation of similar magnitude, can result in a rotation whose axis is far from the axes of either original rotation. Thus the uncertainty in the position of the pole for small rotations is large, and for large rotations (where a small deviatoric rotation can significantly degrade the fit) smaller.

[49] For older times, it is apparent on Figure 13b that the uncertainty regions for our moving hot spot reconstructions are smaller than those for fixed hot spots. This is because the fit of our preferred motion model is inherently better than the fit for fixed hot spots, and this is apparent in our calculated tracks.

[50] One drawback to our approach of fitting statistically independent finite rotations for successive time steps is that there is no mechanism for smoothing the resulting plate motion. By assuming a linear

Table 2. Absolute Plate Rotations and Uncertainties Based on Moving Hot Spots

| Age	Lat.	Long.	Angle	κ	$\kappa-$	$\kappa+$	cov(u)		
10	46.19	−87.86	−1.92	0.92	0.28	1.95	9.94e − 5	−3.80e − 6	−1.18e − 6
							−3.80e − 6	2.84e − 5	−2.30e − 5
							−1.18e − 6	−2.30e − 5	8.68e − 5
20	36.43	−29.41	−4.11	3.19	0.96	6.74	2.30e − 4	2.64e − 6	2.72e − 6
							2.64e − 6	1.15e − 4	−1.20e − 4
20	45.23	−78.55	−3.99	Interpolated 10−30[a]			2.72e − 6	−1.20e − 4	3.18e − 4
30	43.54	−69.67	−6.05	3.31	0.99	7.00	9.89e − 5	2.14e − 5	−3.56e − 5
							2.14e − 5	8.19e − 5	−6.45e − 5
							−3.56e − 5	−6.45e − 5	1.18e − 4
40	44.56	−54.31	−8.08	0.60	0.21	1.9	6.39e − 4	−9.58e − 5	−3.09e − 4
							−9.58e − 5	1.54e − 4	−2.27e − 5
							−3.09e − 4	−2.27e − 5	3.49e − 4
50	36.97	−58.90	−10.26	1.24	0.43	2.47	7.60e − 4	−1.29e − 4	−4.44e − 4
							−1.29e − 4	1.65e − 4	−1.35e − 5
							−4.44e − 4	−1.35e − 5	4.53e − 4
60	23.73	−42.14	−12.53	2.31	0.80	4.59	1.61e − 3	8.69e − 5	−6.22e − 4
							8.69e − 5	6.07e − 4	−2.63e − 4
							−6.22e − 4	−2.63e − 4	7.51e − 4
70	43.81	−71.61	−12.30	1.88	0.56	3.97	7.94e − 4	−3.69e − 5	−4.10e − 4
							−3.69e − 5	2.39e − 4	−9.30e − 5
70	20.74	−39.07	−13.77	Interpolated 60−90[a]			−4.10e − 4	−9.30e − 5	5.35e − 4
80	40.89	−62.28	−14.45	0.88	0.26	1.86	6.31e − 4	6.65e − 5	−3.70e − 4
							6.65e − 5	2.70e − 4	−1.35e − 4
80	17.69	−36.11	−15.00	Interpolated 60−90[a]			−3.70e − 4	−1.35e − 4	4.20e − 4
90	14.60	−33.26	−16.24	2.47	0.60	5.66	5.47e − 4	−9.38e − 5	5.78e − 6
							−9.38e − 5	1.18e − 4	−7.96e − 5
							5.78e − 6	−7.96e − 5	5.36e − 4
100	14.40	−29.63	−20.08	3.25	0.784	7.43	2.41e − 4	−1.79e − 5	1.48e − 5
							−1.79e − 5	3.16e − 4	−1.69e − 5
							1.48e − 5	−1.69e − 5	1.92e − 4
110	9.34	−31.77	−25.53	2.24	0.54	5.11	4.29e − 4	1.33e − 4	1.48e − 5
							1.33e − 4	2.35e − 4	1.06e − 4
110	15.72	−28.32	−24.9	Interpolated 100−120[a]			1.48e − 5	1.06e − 4	2.89e − 4
120	17.03	−27.00	−29.72	9.06	0.65	28.25	7.81e − 4	3.73e − 4	4.38e − 4
							3.73e − 4	6.44e − 4	4.17e − 4
							4.38e − 4	4.17e − 4	5.87e − 4

[a] Interpolated rotations for smooth plate motion model. See text for discussion.

age progression between dated sample points, we implicitly generate a nonsmooth age progression along the hot spot track. To avoid this problem an interpolative smoothing technique could be applied for a given hot spot track age progression, which would however affect our assumption of the independence of each finite rotation. The lack of imposed smoothness on our set of finite absolute plate rotations becomes apparent in our 20, 70, 80 and 110 Ma rotations, which generate artifacts in terms of implausible abrupt changes in the rates and/or directions of absolute plate motion, for which there is no independent evidence (for example a sudden deceleration of plate motion over a 10my time interval followed by an acceleration to the previous rate). In order to create an African absolute plate

motion path in which such artifacts are minimized, we have generated interpolated rotations for 20, 70, 80 and 110 Ma based on the 10/30, 60/90 and 100/ 120 Ma rotations; this generates a smoother and more plausible plate motion history. The uncertainties in these interpolated poles are a combination of the uncertainties in their two bounding rotations.

5. Discussion

[51] We calculated the evolution of several hundred conduits in our interactive evolutionary computations, and several consistent features are worthy of a specific mention. First, it is quite difficult to minimize the motion of the main Indo-Atlantic plumes in the period 0–60 Ma. This is necessary, however,
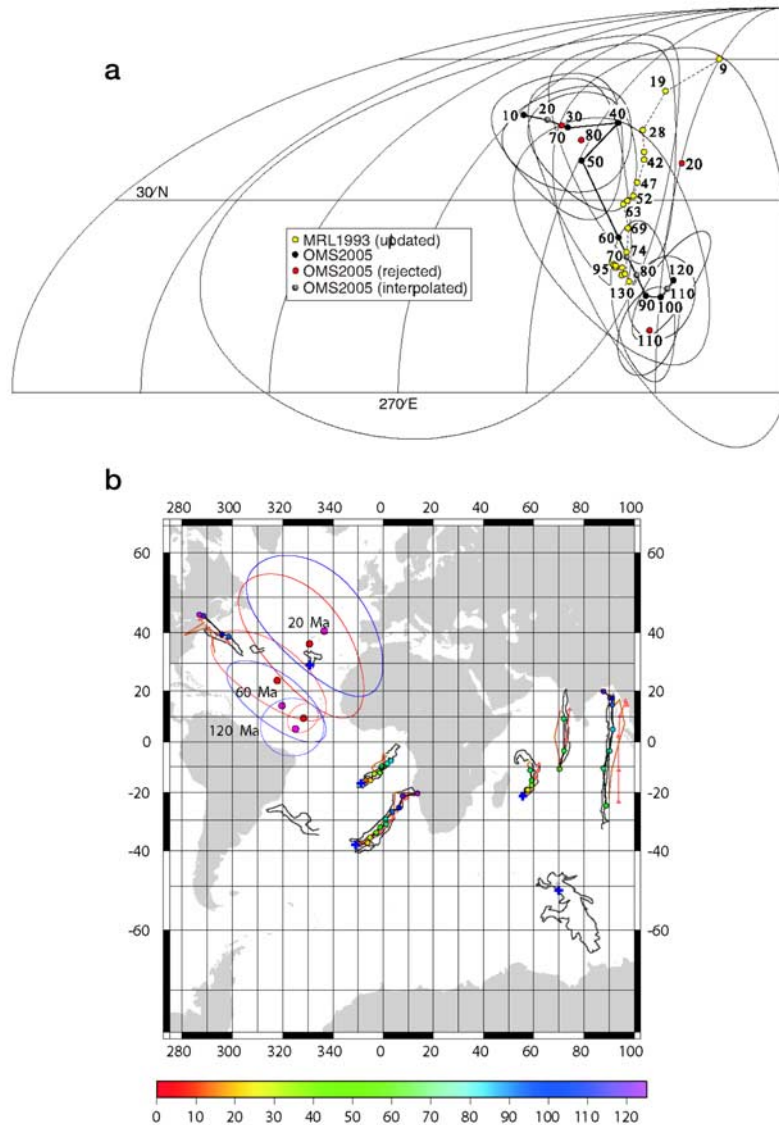
Figure 13. (a) Rotation poles for 10–120 Ma based on our moving hot spot model (OMS2005), including fitted poles that result in unacceptable spikes in our polar wander path (red dots) and our interpolated poles (hollow circles). The uncertainty regions are for our original poles (Table 2). The rotation poles of *Müller et al.* [1993] are also shown for comparison (yellow dots). (b) Predicted tracks of our fixed (brown) and moving (colored circles) hot spot reconstructions for the African plate at 10 Myr intervals. The fixed model has difficulty fitting the Ninetyeast Ridge and New England seamount chain for older times. Assumed present position of hot spots shown as blue crosses. Also shown are the predicted tracks of *Müller et al.* [1993] (red lines) at 10 Myr intervals for our assumed present-day positions. The best fit poles for 20, 60, and 120 Ma are shown, with fixed hot spots poles in blue and moving in red. The latitude-longitude projection of the confidence region of each pole is also shown (red for moving hot spots, blue for fixed). The large uncertainty of the 20 Myr rotation reflects the small angle of this rotation; the smaller uncertainties for older times are due to smaller deviatoric rotations being able to significantly degrade the fit for these larger-angle rotations (see text). The uncertainties for the fixed hot spot model for older times are consistently larger than for the moving model, reflecting the poorer fit of fixed hot spots. Note the uncertainties in the pole position do not directly equate to rotational uncertainties: statistically different rotations can have overlapping uncertainty ellipses for their poles (see text).

for an acceptable fit to the hot spot tracks. In particular, we obtain a consistent northeast motion of Reunion in many of these models, and a southwest drift of Tristan da Cunha (see Figures 9–11). This motion is due to a large-scale lower mantle

upwelling under Africa, which exerts a first-order effect on the mantle flow field, and hot spot motions in this region. The motion of Reunion is minimized by assuming hotter internal conduit temperatures, and subsequently lower viscosities (5e18 Pas), of

the Reunion plume. Tristan da Cunha is somewhat more problematic. A first-order question is why this long-lived, fairly strong plume is not imaged by the model of *Montelli et al.* [2004]? The problem is not likely a resolution problem (R. Montelli, personal communication, 2004). One possibility is that the plume does not have a source region in the lower mantle. This seems unlikely, given its strength over time, and its DUPAL signature [*Dupré and Allègre*, 1983]. Another explanation is that we are currently seeing the end of the lifespan of the Tristan plume; the conduit no longer exists, or extends to the lower mantle, and Tristan da Cunha and Gough Islands represent the tail-end volcanic activity of the plume. Given its age (∼124 Myr) this seems a reasonable explanation. A similar argument can be made for the Great Meteor plume. Our ability to model the 90–120 Ma evolution of the Tristan da Cunha and Great Meteor hot spots is limited by the uncertainties in our "backward-convection" calculations; we obtain this consistent southward drift only in some of our models. The drift is likely to be a real feature for the Great Meteor hot spot, as *Van Fossen and Kent* [1992] present differential paleolatitudes for White Mountains and the rest of North America, and show that TPW is not sufficient to explain the paleolatitudes of both the Tristan da Cunha and Great Meteor hot spots.

[52] The interpreted tilts of the *Montelli et al.* [2004] model are somewhat subjective, in that the magnitude of the anomalies in the lower mantle is small, and spread over a large area. We have digitized what we believe is the center of the hot anomaly at depth, and this interpretation fits well with our modeled conduit tilts. The strong conduit tilts exhibited by Kerguelen and Tristan da Cunha give rise to some interesting behavior. First, the Crozet plume seems to be a diapir of the Kerguelen plume; they both share a common source at depth. Laboratory experiments [e.g., *Olson and Singer*, 1985] show that diapirs can form from instabilities off strongly tilted conduits. The critical tilt determined experimentally is around ∼60 degrees. We argue that in the mantle, strong depth, temperature and stress related dependent effects, large differential shears, and complicated dynamic histories result in a realistic critical tilt significantly less than this. For example, our modeled conduit for Kerguelen is inclined on average at 53.4 degrees to the vertical (similar to the observed tilt from tomography), and it appears to have formed a secondary diapir in the Crozet plume. Tristan is similarly tilted if we assume a D″ source. While the plume is not imaged, and it is possible we are

observing the tail-end of the plume's activity, it may have also produced secondary diapirism along its conduit. The Vema seamount has been dated at around ∼18 Ma [*O'Connor and le Roex*, 1992], and lies to the South of the Walvis Ridge (see Figure 12b). We suggest that this may also be a secondary diapir of a strongly tilted Tristan plume.

[53] The construction of 95% uncertainty ellipsoids for our absolute plate rotations allows us to evaluate the statistical significance of differences between fixed and moving hot spot reference frames. Introducing hot spot motion into absolute plate motion models can be a two-edged sword; it may improve the fit of hot spot tracks for some motion models, while other plume motion models may significantly degrade it. In our case, we have attempted to independently constrain the amount of plume motion using paleomagnetic, tomographic, and geological constraints. To judge the significance of this motion, we use a statistical test to determine if there is a significant difference between our fixed and moving hot spot reference frames. The details of this test are discussed by *Kirkwood et al.* [1999] and outlined in Appendix A. We first tested that ratio of rotation quality factors $\hat{\kappa}$ for each time interval was not significantly different from one, for our fixed and moving hot spot rotations. The quality factor $\hat{\kappa}$ relates the uncertainties assigned to the data to their true estimates. The parameter $\hat{\kappa}$ indicates whether the assigned uncertainties are correct ($\hat{\kappa} \sim 1$), underestimated ($\hat{\kappa} \ll 1$) or overestimated ($\hat{\kappa} \gg 1$). The uncertainties of two rotations can be compared/combined if their quality factors $\hat{\kappa}$ are similar. We then determined the F statistic, used to compare variances between two normally distributed data sets, for the degrees of freedom (df) of each rotation: $F_{0.95}(3,df)$. This is plotted as the red line in Figure 14. Since we use the same data for both our fixed and moving rotations (for a given time), the degrees of freedom are identical for both.

[54] We then combined the moving and fixed hot spot rotations, with the sign of one of the angles of rotation reversed. Hence, if the two rotations are identical, the combined rotation should be the identity. We used the program ADDROT [*Kirkwood et al.*, 1999] for this purpose, which also combines the uncertainties in both rotations, and used the program PVAL [*Kirkwood et al.*, 1999] to ascertain whether this rotation is significantly different from the identity, and produce an F statistic based on this (the formula is given in Appendix A). Both programs are available online, as listed in Appendix A.
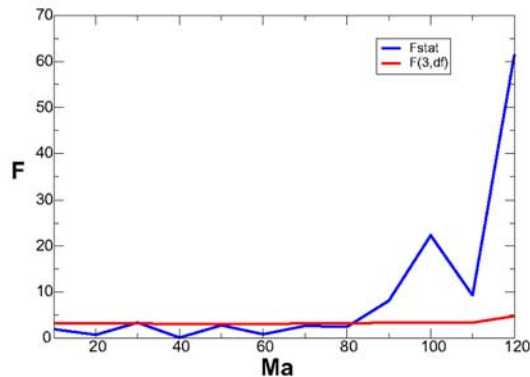
Figure 14. The value of the F statistic F(3,df) for the number of degrees of freedom used in each reconstruction df, shown as the red line. The F statistic for each time is shown as the blue line. This is derived from a combination of the fixed and moving rotation (the one with the sign reversed), which is then tested for its significance from the identity used the program PVAL (see text). The combined rotation is significantly different than identity for ages older than 80 Ma, signifying that our moving hot spot reference frame is only significantly different from our fixed one for times greater than 80 Ma.

The F statistic is plotted as the blue line in Figure 14. As can be seen, for most times it is less than $F_{0.95}(3,df)$. For these times, there is no significant difference between the fixed and moving hot spot rotations. For times greater than 80 Ma, however, the F statistic of the combined rotation is greater than $F_{0.95}(3,df)$, and hence there is a significant difference between our fixed and moving rotations. For our hot spot motion model, there is no significant difference between fixed and moving hot spot reference frames for times 80 Ma or younger; it is only for times older than this that the integrated motion becomes significant. In other words, the motion of hot spots is not discernible above the uncertainties in the data for times less than ∼80 Ma. The one anomaly in Figure 14 is at 30 Ma, when the combined rotation F statistic and $F_{0.95}(3,df)$ are of similar magnitude.

[55] Figure 15 shows reconstructions for the absolute African rotations in Table 2, and a compilation of relative plate motion models [*Gaina et al.*, 2003; *Heine et al.*, 2004; *Müller and Roest*, 1992; *Müller et al.*, 1993; *Nürnberg and Müller*, 1991; *Royer and Chang*, 1991; *Royer and Gordon*, 1997; *Royer and Sandwell*, 1989; *Royer et al.*, 1992; *Shaw and Cande*, 1990]. The boundary between oceanic and continental defines the filled orange areas, and coastlines, major tectonic units and features, and major bathymetric features of tectonic origin

are plotted. The color scale represents the density anomalies in the transition zone, at 640 km depth. These are from the *Su et al.* [1994] model, with other details as in our preferred hot spot motion model. The density anomalies were advected back to 120 Ma, with a filtering of higher harmonics of density anomalies with time to prevent runaway instabilities developing. Note the different scales for each time. The calculated position of the hot spots used in this study through time are shown as red circles. A long-lived low-density anomaly exists under Africa for most of the simulation. The reconstructions do not differ substantially from previous models assuming fixed hot spots for times younger than 90 Ma. Major differences occur at times older than 90 Ma. At these times, the hot spots in our preferred model are further north than their present locations. The result is that Africa is likewise further north than in fixed hot spot reconstructions. This has some important implications. First, our fit of the Kerguelen plume to the present position of the Rajmahal Traps is good. This was not the case in previous fixed-hot spot models, for realistic present positions of the Kerguelen hot spot. This is in part due to the more northward position of the hot spot at this time, but also a consequence of our model. The variation in African paleolatitudes we conclude based on our model has important implications for TPW curves. A case in point is the North American APW standstill between 90 and 120 Ma. *Besse and Courtillot* [2002] concluded that the apparent standstill in this period was due to the TPW and absolute plate motion contributions to the observed paleolatitudes canceling out. In our model, the magnitude of TPW required to give an APW standstill is much less.

[56] We evaluate the paleolatitudinal agreement between the absolute plate rotations from our best fit moving hot spot model with paleomagnetic data by means of a comparison with the global apparent polar wander path from *Torsvik and Van der Voo* [2002] (Figure 16). The *Torsvik and Van der Voo* [2002] APWP has been slightly modified by using the same relative plate motion parameters to rotate paleomagnetic poles from all plates involved into an African reference frame, so that no artifacts are introduced by different sets of relative plate motion parameters. Their modified African APWP is then rotated into our moving mantle reference frame (Table 2) to compute great circle distances between the two reference frames. Compared with a fixed hot spot reference frame, misfits are reduced uniformly for most of the Tertiary and for times older
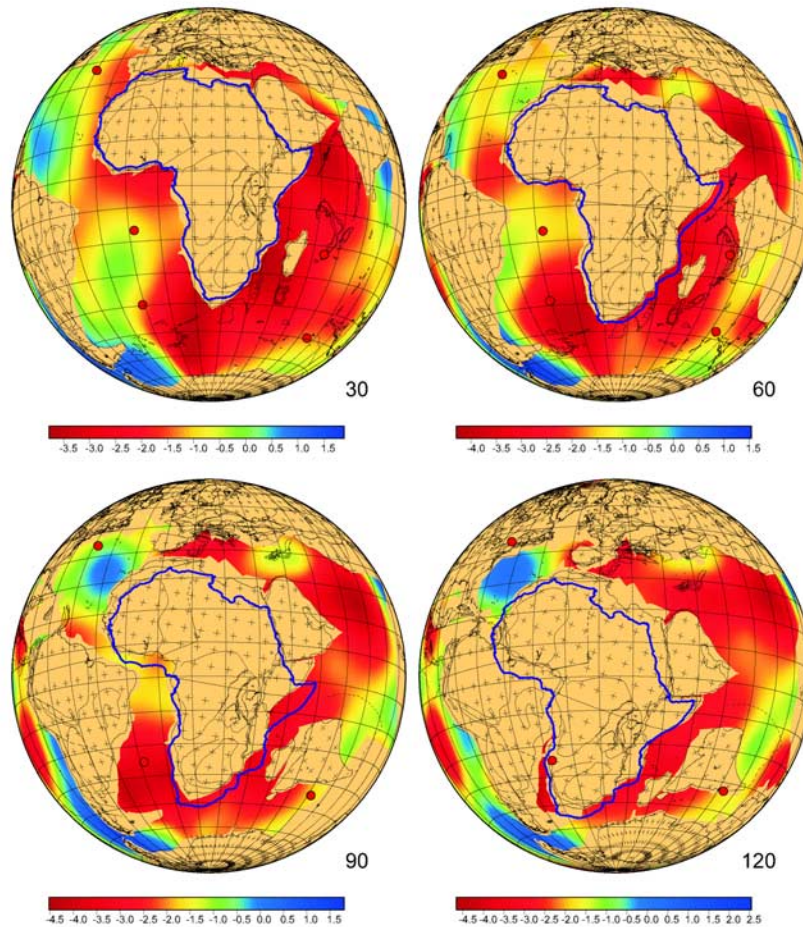
Figure 15. Reconstructed positions of Africa for times shown based on our moving hot spot reference frame (Table 2). Other plates are based on a compilation of relative plate motion models [*Müller and Roest*, 1992; *Müller et al.*, 1993; *Nürnberg and Müller*, 1991; *Royer and Chang*, 1991; *Royer and Gordon*, 1997; *Royer and Sandwell*, 1989; *Royer et al.*, 1992; *Shaw and Cande*, 1990]. Shown are the coastlines, major geological units and tectonic bathymetry features (black lines), continent-ocean boundary (filled orange areas), and past positions of hot spots. Density anomalies in the transition zone (∼640 km) for our preferred flow field model are also shown (see text, and note the scale change at different times). Also shown are our African reconstructions for our fixed hot spot rotations (blue outline; see online auxiliary material)[1].

than 100 Ma. The origin of the misfit peak at 80 Ma is unclear.

[57] Lastly, Figure 17 shows predicted Hawaiian tracks, in 10 Myr intervals, for both our fixed hot spot model (green track), and for our moving hot spot model (red tracks). The absolute motion of the Pacific plate was derived from our Indo-Atlantic/African rotations, adding the relative plate rotations through the plate circuit Africa-East Antarctica-West Antarctica-Pacific using the relative plate motion model of *Gaina et al.* [2003]. An example of our modeled motion of the Hawaiian plume for the last 80 Myr is also shown. This model is similar to Figure 12; we use the S12WM13 tomography model, our preferred viscosity model (v42), and

our preferred thermodynamic parameters. We have, however, included unrealistically low conduit viscosities (10^{16} Pas); this was required to obtain a south-southwest average motion of the Hawaiian plume, in accord with paleolatitude estimates [*Tarduno and Cottrell*, 1997]. The discrepancy between the Indo-Atlantic and Pacific hot spots is obvious for times greater than 40 Ma. While it is not the purpose of this paper to analyze the causes of this discrepancy, we do note that a method of addressing the uncertainties in hot spot reconstructions will be necessary in clarifying this outstanding
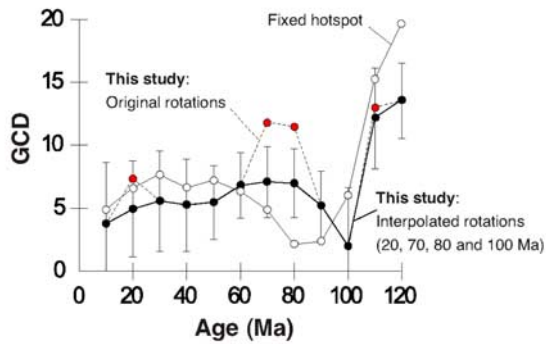

Figure 16. Global apparent polar wander path of *Torsvik and Van der Voo* [2002] (geocentric-axial-dipole based and adjusted for relative plate motions used in this paper) rotated into our mantle frame (Table 2). GCD is great circle distance in degrees between the two reference frames. Error bars correspond to 95% confidence regions of global apparent polar wander path in African coordinates. Compared with a fixed hot spot frame [*Müller et al.*, 1993], misfits are reduced uniformly for the Tertiary and for times larger than 100 Ma. Note that our fixed hot spot model (used in Figure 14) is significantly different than that of *Müller et al.* [1993].

problem. We have projected the confidence regions for our reconstructed points for our moving hot spot model in Figure 16. These are based solely on our African rotations; we have not combined the uncertainties with relative plate motion data, and so these underestimate the total uncertainties. Nonetheless, they show that our model is consistent with the Pacific hemisphere, for a given motion of the Hawaii hot spot, within the uncertainties of our reconstructions, without fixing the Pacific Plate to the Lord Howe Rise during the opening of the Tasman Sea. The latter option represents the preferred kinematic model by *Steinberger et al.* [2004] to model the bend in the Hawaiian-Emperor chain. Our results suggest that there are alternative model options to reconcile the available data from Pacific and Atlantic-Indian hot spot tracks with paleomagnetic data. The key to help resolve this problem lies in better understanding the plate boundary evolution and plate deformation east of the Lord Howe Rise and between East and West Antarctica. Interestingly, the preferred viscosity model 42 has much lower viscosities in the lower mantle, but somewhat higher viscosities in the upper mantle than the preferred model of *Steinberger and O'Connell* [1998]. While this is more consistent with geoid constraints, *Steinberger and O'Connell* [1998] found that, in the Pacific hemisphere, a sufficiently low viscosity below the lithosphere is required in order to prevent plumes from being tilted too

strongly due to shear flow related to plate motions. Conversely, high viscosities in the lower mantle were required in order to obtain sufficiently slow hot spot motions. In the African hemisphere, plate motions are slower; therefore sublithospheric viscosities are not required to be so low. Also, many of the plumes considered here are located in regions of large-scale upwellings. Therefore their position remains relatively stable even with a not so high lower mantle viscosity. The preferred viscosity structure of this paper might therefore correspond to the African region, where the plumes mostly considered in this paper are located, and which is characterized by a lower mantle that is hotter than the global average. Results obtained by using it for plumes in other regions, such as Hawaii, should therefore not be overinterpreted.

6. Conclusion

[58] Large discrepancies exist between predicted hot spot tracks in the Indo-Atlantic and Pacific hemispheres for fixed hot spot models. This suggests motion between these hot spot groups, and evidence from individual hot spots seems to suggest significant hot spot motion. We model the motion of some of the major Indo-Atlantic hot spots for which we have good temporal coverage. We use an interactive evolutionary approach to simulate the mantle flow field and hot spot motion back through time, which uses observations to constrain the models. We present a method for
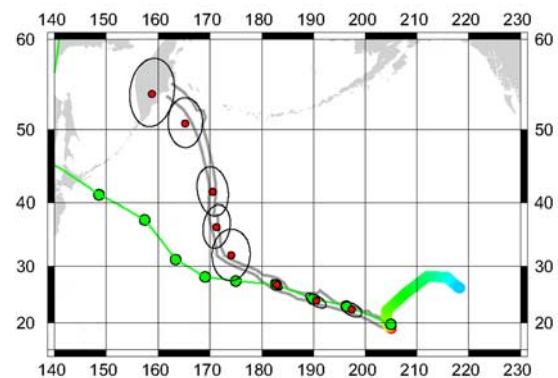
Figure 17. Predicted tracks at 10 Myr intervals for our fixed hot spot model and a fixed Hawaii hot spot (green circles), and for our moving Indo-Atlantic hot spot model (Table 2), for our modeled Hawaii motion (shown for 80 Myr, similar to Figure 14 but with lower conduit viscosities (10^{16} Pas)). Confidence regions are projected from the covariance matrix of our African rotation for our moving hot spot model. The digitized Hawaiian track is shown in gray.

constraining the uncertainties in hot spot reconstructions, and present new African rotations relative to a moving hot spot reference frame for the last 120 Myr. These rotations produce a good fit to hot spot tracks, calculated hot spot motions are consistent with paleolatitudinal constraints, and calculated conduit tilts are consistent with those imaged tomographically. We show that the moving and fixed hot spot reference frames are not different above the level of their uncertainties until 80 Ma, and for a specific model of calculated Hawaiian motion, the discrepancy between the Indo-Atlantic and Pacific hot spot reference frames is not discernible above the level of the uncertainties in the absolute plate rotations.

Appendix A

A1. Some Geometrical Properties of Spherical Data

[59] Uncertainties in hot spot reconstructions have been rarely addressed. Our motivation in this analysis is to quantitatively determine uncertainty for absolute hot spot–track reconstructions which conforms with the method of constraining uncertainties presented by *Chang* [1987] for relative plate rotations. While the discussion follows closely from *Chang* [1987], we find a clear description of the geometrical properties of spherical data useful in our further elaboration of rotational uncertainties.

[60] Suppose we have a data set distributed on a sphere, such as a digitized segment of a hot spot track as shown in Figure A1. Each point is described by a latitude λ and longitude θ, which can be converted to a Cartesian (x, y, z) triplet by the transforms:

$$\mathbf{x} = \mathbf{rcos}\lambda\mathbf{cos}\theta,$$

$$\mathbf{y} = \mathbf{rcos}\lambda\mathbf{sint}\theta, \quad (A1)$$

$$\mathbf{z} = \mathbf{rsin}\lambda.$$

[61] Here r is the radius of the sphere which we will assume to be unity in the following. The distribution of these points can be described by a position matrix $\sum$, where $\sum$ is given by

$$\sum = \frac{1}{n}\sum_{i=1}^{n}\begin{pmatrix} x_i^2 & xy_i & xz_i \\ xy_i & y_i^2 & yz_i \\ xz_i & yz_i & z_i^2 \end{pmatrix} \quad (A2)$$

Here i corresponds to each data point, and the total number of points is n. The position matrix for the

data set in Figure A1a is shown in Figure A1b. This position matrix has several properties which describe the distribution of the original data on a sphere. An eigen-decomposition of the matrix $\sum$ gives us three eigenvectors, corresponding to the position of three points on the sphere as shown in Figure A1a. The eigenvector S(3) corresponding to the largest eigenvalue (i.e., 0.999) is situated in the center of the data set, and so describes the mean position of the data on a sphere. Since the corresponding eigenvalue is close to 1, this tells us that the data lie close to a point (i.e., the S(3) eigenvector), relative to the radius of the sphere. The second eigenvector S(2) describes a point ninety degrees away from the first. Since S(2)'s corresponding eigenvalue $\Lambda(2)$ is much larger than the smallest eigenvalue $\Lambda(1)$ (0.035versus2.818e-5), it follows that the data approximate a great circle segment, which passes through the S(3) and S(2). The eigenvector S(1) corresponds to the smallest eigenvalue, and lies ninety degrees away from the great circle segment. Thus S(1) represents the normal to the great circle segment. In the limit that the data fall exactly on a great circle segment described by S(3) and S(2), then the eigenvalue $\Lambda(1)$ will approach zero.

A2. A Description of Hellinger's Criterion of Fit

[62] The Hellinger criterion was developed by *Hellinger* [1981] to estimate an unknown relative plate rotation by reconstructing conjugate fracture zone and isochron segments. In this method, the segments are considered to be great circle segments. Deviations from this assumption are assumed to be negligible compared to the inherent errors in the data.

[63] Isochrons are generally reconstructed from magnetic anomaly identifications, compiled from a number of ship tracks which cross the magnetic anomaly lineation. Fracture zones are generally reconstructed in a similar way, from gravity or bathymetry measurements. More recently, satellite gravity and altimetry data [e.g., *Smith and Sandwell*, 1997] have mapped the ocean floor in unprecedented detail, aiding the identification of fracture zones. Thus both data sets have inherent positional errors, from which it is possible to construct an uncertainty region for a rotation based on them.

[64] Following from *Chang* [1988], we assume that we have two conjugate data sets (shown in Figure A2), $u_{ij}(j = 1,...,m_i)$ and $v_{ik}(k = 1,,n_i)$. Here i denotes the ith great circle segment, and m_i and n_i
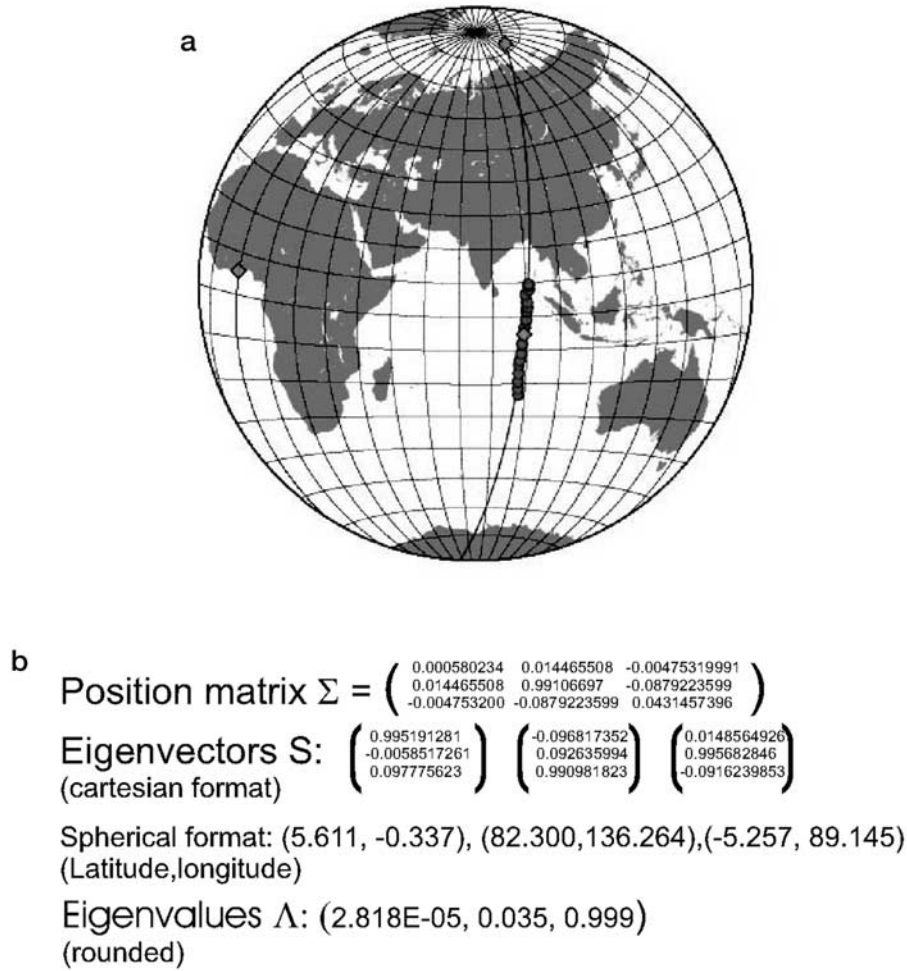
Figure A1. Distribution on a typical geophysical data set on a sphere, here a digitized section of the Ninetyeast Ridge (red circles). The position matrix of this data set, as described in the text, is shown. The three eigenvectors of this position matrix are listed in Cartesian and geographical coordinates and correspond to the blue diamonds on the map. Their respective eigenvalues are shown; the eigenvectors corresponding to the two largest eigenvalues describe a great circle which passes through the data (shown).

the number of data points on the ith great circle segment. If $\eta_1,\ldots,\eta_s$ represent normals to the great circle segments on one side, then $A_o\eta_1,\ldots,A_o\eta_s$ represent the normals to the these same segments on the conjugate side, for an unknown rotation A_o. The Hellinger criterion is a least squares estimate of the unknown rotation and the set of normals $\eta = \eta_1,\ldots,\eta_s$. It states that the best fit rotation A minimizes

$$r(A, \eta) = \sum_{i,j}\left(\frac{u_{i,j}^t\eta_i}{\sigma_{i,j}}\right)^2 + \sum_{i,k}\left(\frac{v_{i,k}^tA\eta_i}{\tilde{\sigma}_{i,j}}\right)^2. \quad (A3)$$

Note that σ and $\tilde{\sigma}$ denote the estimated errors in the data. It was shown by Hellinger that this can be written as

$$r(A, \eta) = \sum_i \eta_i^t\left(\sum_i^a + A^t\sum_i^b A\right)\eta_i, \quad (A4)$$

Where

$$\sum_i^a = \sum_j \frac{u_{i,j}u_{i,j}^t}{\sigma_{i,j}^2} \text{ and } \sum_i^b = \sum_j \frac{v_{i,j}v_{i,j}^t}{\tilde{\sigma}_{i,j}^2}.$$

[65] This leads to an important observation. Consider the matrix $(a\sum_i + A^t\sum_i^b A)$ (bracketed part of equation (A4)). This matrix represents essentially the position matrix of the data, rotated onto the same plate for a given rotation A. If we consider just one section; and if we know the rotation, then the reconstructed data should result in a data set that approximates a great circle segment (i.e., the position matrix of one side, plus the position matrix of the other conjugate side rotated onto the first plate, should be a great circle). In other words, the two eigenvectors of $(a\sum_i + A^t\sum_i^b A)$ corresponding to
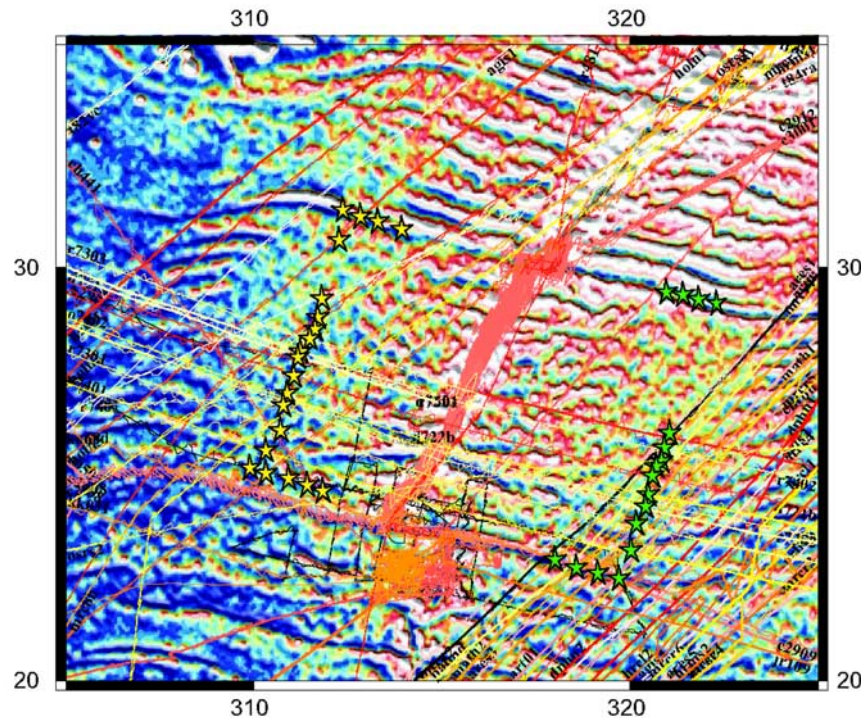
Figure A2. An example of the Hellinger criteria of fit for relative plate motions. The data sets used are digitized isochrons and fracture zone segments. The Hellinger criteria assumes the individual segments can be approximated by great circle segments and that the best fit rotation is that which minimizes the misfit of these reconstructed conjugate segments from great circles.

the largest eigenvalues will describe a great circle segment which approximates the reconstructed data. The smallest eigenvalue's eigenvector will describe a point 90 degrees away from these two. Hence the smallest eigenvalue's eigenvector is chosen as the normal to the great circle segment $\hat{\eta}_i(A)$ (cap denotes that it is an estimate). Also, the smallest eigenvalue for each segment represents a measure of the misfit of the data from a great circle, and one can envisage a method of estimating the best fit rotation by minimizing the sum of this 'misfit' over all the segments. Specifically, r is minimized for any given A by choosing the normal $\hat{\eta}_i(A)$ to be the eigenvector corresponding to the smallest eigenvalue of $(\sum_i^a + A^t \sum_i^b A)$.

A3. Chang's Method for Estimating Uncertainties in Relative Plate Rotations

[66] Fundamental to the discussion of uncertainties in plate rotations is the method for parameterizing the rotations themselves. There are many methods of parameterizing rotations [*Chang et al.*, 1990], including the latitude, longitude of the axis of rotation, and the angle of rotation (λ, θ, ρ), three

Euler angles (α, β, γ), a Cartesian vector describing the axis of rotation, with length equal to the rotation angle, or unit quaternions. While it is possible to derive some measure of uncertainty for any of these parameterizations, many are difficult to visualize. For example, uncertainties in latitude, longitude and rotation angle are generally portrayed by an error ellipse around the pole of rotation, describing the projection of a 3-D error ellipsoid onto the latitude-longitude plane. Such a projection can be misleading; uncertainties in the rotation axis are much larger for small rotations than for large ones (i.e., a small rotation, plus a small deviatoric rotation can give a resulting rotation axis relatively far from that of the two original rotations).

[67] More problematic is the combination of uncertainties when two rotations are added. For example, to combine rotations **A** and **B**, the result is the product **AB**. As noted by *Chang et al.* [1990], the matrix **AB** is not, in general, the matrix given by the Cartesian-form rotation $\mathbf{R}(\lambda_a + \lambda_b, \theta_a + \theta_b, \rho_a + \rho_b)$. Thus the uncertainty in **AB** becomes awkward to express in these formulations.

[68] *Molnar and Stock* [1985] provided a fundamental insight into the formulation of these rotational uncertainties. Namely, the primary goal of rotational uncertainties is not to understand the uncertainty in the pole position or angle, but rather to know uncertainties in the reconstructed positions of the plates. They noted that a measure of the uncertainty of a rotation is how much a small deviatoric rotation, added to the best fit rotation, affects the fit of the data. If a small deviatoric rotation significantly degrades the fit of the data, the uncertainty in the rotation is small. Conversely, if a small deviatoric rotation to the best fit rotation doesn't significantly degrade the fit, the uncertainty in the rotation is larger. This argument was continued by *Chang et al.* [1990]. They noted that the best way to parameterize a rotation was not in uncertainties in the rotation values themselves, but rather by defining a group of small rotations $\Delta \mathbf{R}$, which can be added to the estimated rotation $\hat{\mathbf{R}}$ without significantly degrading the fit. This eliminates the problem with parameterizing the rotation itself (any parameterization will do), and the problem becomes choosing a parameterization for the group of small rotations $\Delta \mathbf{R}$ which distorts it least. This formulation is known as a moving parameterization, since rotations close to $\hat{\mathbf{R}}$ are parameterized by their differences from $\hat{\mathbf{R}}$.

[69] The choice of parameterization of *Chang* [1988] is the moving exponential parameterization. The basis of this parameterization is a three-vector $\mathbf{u} = [t_1, t_2, t_3]^t$. The rotation $\Phi(\mathbf{u})$ represents a right-hand rule rotation of $|\mathbf{u}| = \sqrt{t_1^2 + t_2^2 + t_3^2}$ radians around the axis $\mathbf{u}/|\mathbf{u}|$. If we let

$$\mathbf{T} = \begin{pmatrix} 0 & -t_3 & t_2 \\ t_3 & 0 & -t_1 \\ -t_2 & t_1 & 0 \end{pmatrix}, \qquad (A5)$$

then it follows that

$$\Phi(\mathbf{u}) = \sum_{r=0}^{r=\infty} \mathbf{T}^r / r! = e^{\mathbf{T}}. \qquad (A6)$$

As noted by *Chang* [1988], this sum reduces to

$$\Phi(\mathbf{u}) = \mathbf{I} + \frac{\sin\|\mathbf{u}\|}{\|\mathbf{u}\|}\mathbf{T} + \frac{1 - \cos\|\mathbf{u}\|}{\|\mathbf{u}\|^2}\mathbf{T}^2. \qquad (A7)$$

To borrow an example from *Chang* [1987], if $\mathbf{u} = [1 \ -2 \ 1]^t$, then $\Phi(\mathbf{u})$ is a right-hand rule rotation of 2.4495 radians (140.3 degrees)

around the axis [0.4082, −0.8165, 0.4082], i.e., (24.09°N,63.43°W). Then

$$\Phi\begin{pmatrix} 1 \\ -2 \\ 1 \end{pmatrix} = \begin{bmatrix} -0.4749 & -0.8505 & -0.2261 \\ -0.3294 & 0.4100 & -0.8504 \\ 0.8160 & -0.3294 & -0.4749 \end{bmatrix}.$$

The advantage of the exponential parameterization is that it represents small rotations near the origin with minimal distortion. Parameterizations such as (λ, θ, ρ) or (α, β, γ) have singularities near the origin and are not suitable in describing small rotations.

[70] The estimated rotation can then be written $\hat{\mathbf{R}} = \mathbf{R}\Phi(\mathbf{u})$. As was shown by *Chang* [1988], $\hat{\mathbf{R}} = \mathbf{R}\Phi(\mathbf{u})$ is equivalent to $\mathbf{R} = \hat{\mathbf{R}} \Phi(-\mathbf{u})$. If we let the perturbation rotation $\Phi(\mathbf{u}) = \mathbf{A}_o^t \mathbf{A}$ (for the real and estimated rotations, respectively), then the uncertainty in our estimated rotation $\mathbf{A_o}$ is given by the covariance matrix cov($\mathbf{u}$). In the real world, the matrix we call cov($\mathbf{u}$) is an estimate of the real covariance matrix of $\mathbf{u}$, and is derived from the data. This is important, in that while $\mathbf{u}$ itself is generally not known, an estimate of its covariance matrix can still be made. The formula and derivations of cov($\mathbf{u}$), as given by *Chang* [1988], are given in section A5.

[71] For a given confidence level of α, the confidence region is defined by all the rotations $\mathbf{R} = \hat{\mathbf{R}} \Phi(\mathbf{u})$ which satisfy the condition

$$\mathbf{u}^t(\text{cov}(\mathbf{u}^u))^{-1}\mathbf{u} < \chi_\alpha^2(3). \qquad (A8)$$

This assumes that the uncertainties have been correctly estimated. A measure of this is the parameter κ, which is estimated by

$$\hat{\kappa} = \frac{N - 2s - 3}{\mathbf{r}(\hat{A}, \hat{\eta})} = \frac{\text{df}(A)}{\mathbf{r}(\hat{A}, \hat{\eta})}. \qquad (A9)$$

Here N is the total number of data points, and s the number of segments. If κ equals 1, then the assigned errors are good estimates. If $\kappa \gg 1$, then the assigned errors are too big; if $\kappa \ll 1$ they are too small. If κ is not known, then equation (A8) becomes

$$\mathbf{u}^t(\text{cov}(\mathbf{u}^u))^{-1}\mathbf{u} < 3F_\alpha(3, N - 2s - 3) \qquad (A10)$$

for an F distribution. This confidence region is a three-dimensional ellipsoid (i.e., the axes are latitude, longitude and angle). This ellipsoid can

be projected onto a latitude-longitude plane using an algorithm described by *Hanna and Chang* [1989].

A4. Comparisons to Other Methods of Measuring Uncertainties

[72] *Molnar and Stock* [1985] introduced a method for estimating the uncertainties in relative plate reconstructions by estimating the size of three small perturbing rotations from the reconstructed data. If a large perturbing rotation does not significantly degrade the goodness of fit, the uncertainty is quite large. Conversely, if a small perturbing rotation degrades the goodness of fit significantly, the uncertainty is quite small. For consistency, *Molnar and Stock* [1985] used three perturbing rotations, known as partial uncertainty rotations (PURs), estimated from the data distribution. The first rotation axis passes through the center of the data distribution. A rotation about this axis will affect the skew-fit of the data; incidentally this is generally the largest uncertainty in reconstructed data. The other two PURs lie ninety degrees from this axis. For relative plate motion data, these rotations test the goodness of fit of fracture zones and isochrons, respectively.

[73] *Chang* [1988] and *Chang et al.* [1990] observed that if one considers the eigenvectors of $(\text{cov}(\mathbf{u}))^{-1}$, these describe three axes at ninety degrees to each other. Their respective eigenvalues constrain the maximum permissible rotation θ about these axes that will degrade the fit of the data to the specified limit:

$$\theta = \sqrt{c/D_j}. \qquad (A11)$$

For the jth eigenvalue, where c equals χ^2_α (3) if $\kappa = 1$, otherwise c = $3F_\alpha(3, \text{df}(A))$, where df(A) is the degrees of freedom of the rotation A.

[74] These rotations are roughly equivalent to the PURs described by *Molnar and Stock* [1985]. Since one is estimated from the plate boundary geometry, and the other from the distribution of data points and their estimated errors, the two will not be identical. However, the analogy is useful for describing what the matrix cov(**u**) actually represents.

A5. Derivation of Chang's Covariance Matrix

[75] The following is a cookbook recipe for deriving Chang's covariance matrix, and the terminology follows that of *Chang* [1988]. For the mathematical basis, and associated theorems, and implicit assumptions, see *Chang* [1988].

[76] We define the following: α_{ij} is the jth unknown point on the ith great circle segment, where the total number of sections is s, and the total number of points on that section is m. The tilde ($\sim$) denotes points on the conjugate plate, the number of points on the conjugate plate is n. N = m + n. η_i is the normal to the ith great circle section. O_i is a 3*1 matrix whose columns form a basis of vectors perpendicular to η_i.

$$\sum_i = \sum_j \kappa_{ij}\, \alpha_{ij}\, \alpha_{ij}^t$$

$$\tilde{\sum}_i = \sum_k \tilde{\kappa}_{ik}\, \tilde{\alpha}_{ik}\, \tilde{\alpha}_{ik}^t$$

$$H_{11} = \sum_i M(\eta_i)A_o^t \tilde{\sum}_i A_o M(\eta_i)^t \; (3 \times 3)$$

$$H_{12} = \left[M(\eta_1)A_o^t \tilde{\sum}_1 A_o O_1 \cdots M(\eta_s)A_o^t \tilde{\sum}_s A_o O_s \right] \; (3 \times 2s)$$

$$H_{21} = H_{12}^t$$

$H_{22} = \text{block\_diagonal}$

$$\left[O_1^t\left(\sum_1 + A_o^t \tilde{\sum}_1 A_o\right)O_1 \cdots O_s^t\left(\sum_s + A_o^t \tilde{\sum}_s A_o\right)O_s \right]$$

Then we define the design matrix X with

$$X^tX = \begin{bmatrix} H_{11} & H_{12} \\ H_{21} & H_{22} \end{bmatrix}.$$

Then we let

$$H_{11.2} = H_{11} - H_{12}H_{22}^{-1}H_{21}.$$

The covariance matrix of Chang is the inverse of $H_{11.2}$. This derivation is performed by the program HELLINGER1, described in more detail by *Kirkwood et al.* [1999], and can be obtained via ftp from http://www.stat.virginia.edu.

A6. Uncertainties of Reconstructed Points

[77] The confidence region for a data point is derived from the covariance matrix for the rotation, but is easier to visualize since it lies uniquely in the latitude-longitude plane. For a data point w and

estimated rotation $\hat{A}$, the confidence region of $\hat{A}w$ is derived from

$$cov(\hat{A}w) = \hat{A}M(w)cov(\mathbf{u})(M(w))^t\hat{A}^t.$$

The confidence region of $\hat{A}w$ is an ellipse characterized with the major axis L_i (i = 1, 2, 3), which is a vector perpendicular to the rotated vector $\hat{A}w$, and the half-length l of the minor axis. Assuming Dj and Zij (i = 1, 2, 3; j = 1, 2, 3) are the eigenvalues and associated eigenvectors of $cov(\hat{A}w)$, then

$$L_i = \sqrt{cD_3}\, Z_{i3}\,(i = 1, 2, 3)$$
$$l = \sqrt{cD_2}$$

If $\kappa_A = 1$, $c = \chi^2_{\alpha(3)}$
Otherwise, if κ_A is estimated, then

$c = 3F_\alpha(3, df(A))$.

This routine is performed by the program PTELLIPSE, described in more detail by *Kirkwood et al.* [1999], and can be obtained via ftp from http://www.stat.virginia.edu.

A7. Fstat Test

[78] For fixed and moving rotations A1 and A2, we need to ascertain whether the combination of the two A3, (where A3 = A1(−A2)) is significantly different from identity. To do this, we must first determine that the ratio of their κ values is not different from 1 at 10% significance; i.e.,

$$F_{0.9}(df_{A1}, df_{A2}) < F = \frac{\hat{\kappa}_{A1}}{\hat{\kappa}_{A2}}.$$

(See *Kirkwood et al.* [1999] for more details.) Next, assuming our estimated κs are equal, we define an F statistic:

$$F = \frac{r_{A3} - (r_{A1} + r_{A2})}{df_{A3} - (df_{A1} + df_{A2})} \times \frac{df_{A1} + df_{A2}}{r_{A1} + r_{A2}}.$$

Now the F statistic for A3, with degrees of freedom df_{A3}, at 95% confidence is $F_{0.95}$ (3, df_{A3}). If this is less than F, i.e., $F_{0.95}$ (3, df_{A3}) < F, then we can say that the rotations A1 and A2 are significantly different at 95% confidence. The routines required to do this are ADDROT and PVAL, both available from http://www.stat.virginia.edu.

Acknowledgments

References

Albers, M., and U. R. Christensen (1996), The excess temperature of plumes rising from the core-mantle boundary, *Geophys. Res. Lett.*, *23*(24), 3567–3570.

Andrews, D. L., and R. G. Gordon (2003), Revised estimate of the Cenozoic motion between the Tristan da Cunha hotspot and the Pacific hotspots, *Eos Trans. AGU*, *84*(46), Fall Meet. Suppl., Abstract V21F-06.

Antretter, M., B. Steinberger, F. Heider, and H. Soffel (2002), Paleolatitudes of the Kerguelen hotspot: New paleomagnetic results and dynamic modeling, *Earth Planet. Sci. Lett.*, *203*, 635–650.

Baksi, A. K. (1999), Reevaluation of plate motion models based on hotspot tracks in the Atlantic and Indian Oceans, *J. Geol.*, *107*(1), 13–26.

Baksi, A. K., T. R. Barman, D. K. Paul, and E. Farrar (1987), Widespread Early Cretaceous flood basalt volcanism in Eastern India: Geochemical data from the Rajmahal-Bengal-Sylhet Traps, *Chem. Geol.*, *63*, 133–141.

Besse, J., and V. Courtillot (2002), Apparent and true polar wander and the geometry of the geomagnetic field over the last 200 Myr, *J. Geophys. Res.*, *107*(B11), 2300, doi:10.1029/2000JB000050.

Boschetti, F., and L. Moresi (2001), Interactive inversion in geosciences, *Geophysics*, *64*, 1226–1235.

Boschetti, F., C. Wijns, and L. Moresi (2003), Effective exploration and visualization of geological parameter space, *Geochem. Geophys. Geosyst.*, *4*(10), 1086, doi:10.1029/2002GC000503.

Bunge, H.-P., C. R. Hagelberg, and B. J. Travis (2003), Mantle circulation models with variational data assimilation: Inferring past mantle flow and structure from plate motion histories and seismic tomography, *Geophys. J. Int.*, *152*, 280–301.

Chaffey, D. J., R. A. Cliff, and B. M. Wilson (1989), Characterization of the St Helena magma source, *Geol. Soc. Spec. Publ.*, *42*, 257–276.

Chang, T. (1987), On the statistical properties of estimated rotations, *J. Geophys. Res.*, *92*, 6319–6329.

Chang, T. (1988), Estimating the relative rotation of two tectonic plates from boundary crossings, *J. Am. Stat. Assoc.*, *83*, 1178–1183.

Chang, T., J. Stock, and P. Molnar (1990), The rotation group in plate tectonics and the representation of uncertainties of plate reconstructions, *Geophys. J. Int.*, *102*, 649–661.

Christensen, U. R., and D. A. Yuen (1985), Layered convection induced by phase transitions, *J. Geophys. Res.*, *90*, 10,291–10,300.

Coffin, M. F., M. S. Pringle, R. A. Duncan, T. P. Gladczenko, M. Storey, R. D. Mueller, and L. A. Gahagan (2002), Kerguelen hotspot magma output since 130 Ma, *J. Petrol.*, *43*(7), 1121–1139.

Conrad, C. P., and M. Gurnis (2003), Seismic tomography, surface uplift, and the breakup of Gondwanaland: Integrating mantle convection backwards in time, *Geochem. Geophys. Geosyst.*, *4*(3), 1031, doi:10.1029/2001GC000299.

Courtillot, V. E., J. Besse, D. Vandamme, R. Montigny, J. Jaeger, and H. Cappetta (1986), Deccan flood basalts at the Cretaceous/Tertiary boundary?, *Earth Planet. Sci. Lett.*, *80*, 361–374.

Curray, J. R., and T. Munasinghe (1991), Origin of the Rajmahal Traps and the 85°E Ridge: Preliminary reconstructions of the trace of the Crozet hotspot, *Geology*, *19*, 1237–1240.

Deckart, K., G. Feraud, L. S. Marques, and H. Bertrand (1998), New time constraints on dyke swarms related to the Parana-Etendeka magmatic province, and subsequent South Atlantic opening, southeastern Brazil, *J. Volcanol. Geotherm. Res.*, *80*(1–2), 67–83.

Duncan, R. A. (1978), Geochronology of basalts from the Ninetyeast Ridge and continental dispersion in the Eastern Indian Ocean, *J. Volcanol. Geotherm. Res.*, *4*, 283–305.

Duncan, R. A. (1984), Age progressive volcanism in the New England seamounts and the opening of the central Atlantic Ocean, *J. Geophys. Res.*, *89*, 9980–9990.

Duncan, R. A. (1990), The volcanic record of the Reunion hotspot, *Proc. Ocean Drill. Program Sci. Results*, *115*, 3–10.

Duncan, R. A. (1991), Age distribution of volcanism along aseismic ridges in the eastern Indian Ocean, *Proc. Ocean Drill. Program Sci. Results*, *121*, 507–517.

Duncan, R. A. (2002), A time frame for construction of the Kerguelen Plateau and Broken Ridge, *J. Petrol.*, *43*(7), 1109–1119.

Duncan, R. A., and R. B. Hargraves (1990), ^{40}Ar/^{39}Ar geochronology of basement rocks from the Mascarene Plateau, the Chagos Bank, and the Maldives Ridge, *Proc. Ocean Drill. Program Sci. Results*, *115*, 43–52.

Duncan, R. A., and D. G. Pyle (1988), Rapid eruption of the Deccan flood basalts at the Cretaceous/Tertiary boundary, *Nature*, *333*, 841–843.

Duncan, R. A., and M. A. Richards (1991), Hotspots, mantle plumes, flood basalts, and true polar wander, *Rev. Geophys.*, *29*(1), 31–50.

Dupré, B., and C. Allègre (1983), Pb-Sr isotope variation in Indian Ocean basalts and mixing phenomena, *Nature*, *303*, 142–146.

Ebinger, C. J., and N. H. Sleep (1998), Cenozoic magmatism throughout east Africa resulting from impact of a single plume, *Nature*, *395*(6704), 788–791.

Ernesto, M., I. G. Pacca, F. Y. Hiodo, and A. J. R. Nardy (1990), Paleomagnetism of the Mesozoic Serra Geral Formation, southern Brazil, *Phys. Earth Planet. Inter.*, *64*, 153–175.

Forte, A. M., and J. X. Mitrovica (1991), Inferences on mantle viscosity from tectonic plate velocities, *Geophys. Res. Lett.*, *18*, 1747–1750.

Frey, F. A., N. J. McNaughton, D. R. Nelson, J. R. deLaeter, and R. Duncan (1996), Petrogenesis of the Bunbury Basalts, Western Australia: Interaction between the Kerguelen Plume and Gondwana Lithosphere?, *Earth Planet. Sci. Lett.*, *144*, 163–183.

Gaina, C., R. D. Müller, B. Brown, and T. Ishihara (2003), Microcontinent formation around Australia, in *The Evolution and Dynamics of the Australian Plate*, edited by R. Hillis and R. D. Müller, *Spec. Pap. Geol. Soc. Am.*, *22*, 399–410.

Gilbert, L. A., and K. A. Foland (1986), The Mont St. Hilaire plutonic complex: Occurrence of excess ^{40}Ar and short intrusion history, *Can. J. Earth Sci.*, *23*, 948–958.

Grand, S. P., R. D. van der Hilst, and S. Widiyantoro (1997), Global seismic tomography: A snapshot of convection in the Earth, *GSA Today*, *7*, 1–7.

Hager, B. H., and R. J. O'Connell (1979), Kinematic models of large scale mantle flow, *J. Geophys. Res.*, *84*, 1031–1048.

Hager, B. H., and R. J. O'Connell (1981), A simple global model of plate dynamics and mantle convection, *J. Geophys. Res.*, *86*, 4843–4867.

Hanna, M. S., and T. Chang (1989), On graphically representing the confidence region for an unknown rotation in three dimensions, *Comput. Geosci.*, *16*, 163–194.

Harada, Y., and Y. Hamano (2000), Recent progress on plate motions relative to hotspots, in *The History and Dynamics of Global Plate Motions*, *Geophys. Monogr. Ser.*, vol. 121, edited by M. A. Richards, R. G. Gordon, and R. D. van der Hilst, pp. 327–338, AGU, Washington, D. C.

Heine, C., R. D. Müller, and C. Gaina (2004), Reconstructing the lost Eastern Tethys Ocean Basin: Convergence history of the SE Asian margin and marine gateways, in *Continent-Ocean Interactions Within East Asian Marginal Seas*, *Geophys. Monogr. Ser.*, vol. 149, edited by P. Clift et al., pp. 37–54, AGU, Washington, D. C.

Hellinger, S. J. (1981), The uncertainties of finite rotations in plate tectonics, *J. Geophys. Res.*, *86*, 9312–9318.

Hofmann, C., G. Feraud, and V. Courtillot (2000), ^{40}Ar/^{39}Ar dating of minerals separates and whole rocks from the Western Ghats lava pile: Further constraints on the duration and age of the Deccan Traps, *Earth Planet. Sci. Lett.*, *180*, 13–27.

Hubacher, F. A., and K. A. Foland (1991), ^{40}Ar/^{39}Ar ages for Cretaceous intrusions of the White Mountain magma series, northern New England, and their tectonic implications, *Geol. Soc. Am. Abstr. Programs*, *23*(1), 47.

Ingle, S., D. Weis, J. S. Scoates, and F. A. Frey (2002), Relationship between the early Kerguelen plume and continental flood basalts of the paleo-Eastern Gondwanan margins, *Earth Planet. Sci. Lett.*, *197*(1–2), 35–50.

Kent, R. W., A. D. Saunders, P. D. Kempton, and N. C. Ghose (1997), Rajmahal basalts, eastern India: Mantle sources and melt distribution at a volcanic rifted margin, in *Large Igneous Provinces: Continental, Oceanic, and Planetary Flood Volcanism*, *Geophys. Monogr. Ser.*, vol. 100, edited by J. J. Mahoney and M. F. Coffin, pp. 145–182, AGU, Washington, D. C.

Kent, R. W., M. S. Pringle, R. D. Mueller, A. D. Saunders, and N. C. Ghose (2002), ^{40}Ar/^{39}Ar geochronology of the Rahmahal Basalts, India, and their relationship to the Kerguelen Plateau, *J. Petrol.*, *43*(7), 1141–1153.

King, S. D. (1995), The viscosity structure of the mantle, *Rev. Geophys.*, *33*(S1), 11–17.

King, S. D., and G. Masters (1992), An inversion for radial viscosity structure using seismic tomography, *Geophys. Res. Lett.*, *19*, 1551–1554.

Kirkwood, B. H., J. Y. Royer, T. C. Chang, and R. G. Gordon (1999), Statistical tools for estimating and combining finite rotations and their uncertainties, *Geophys. J. Int.*, *137*(2), 408–428.

Masters, G., G. Laske, H. Bolton, and A. M. Dziewonski (2000), The relative behavior of shear velocity, bulk sound speed, and compressional velocity in the mantle: Implications for chemical and thermal structure, in *Earth's Deep Interior*, *Geophys. Monogr. Ser.*, vol. 117, edited by S. I. Karato et al., pp. 63–86, AGU, Washington, D. C.

McDougall, I. (1971), The geochronology and evolution of the young oceanic island of Reunion, Indian Ocean, *Geochim. Cosmochim. Acta*, *35*, 261–270.

McDougall, I. (1973), Potassium-argon ages on basaltic rocks from cores from D. S. P. D. Leg 22, Indian Ocean, *Initial Rep. Deep Sea Drill. Program*, *22*, 377–380.

McElhinny, M. W., and P. L. McFadden (1999), *Paleomagnetism: Continents and Oceans*, 386 pp., Elsevier, New York.

Meyerhoff, A. A., and M. Kamen-Kaye (1981), Petroleum prospects of Saya de Malha and Nazareth Banks, Indian Ocean, *AAPG Bull.*, *65*, 1344–1347.

Molnar, P., and J. M. Stock (1985), A method for bounding uncertainties in combined plate reconstructions, *J. Geophys. Res.*, *90*(B14), 12,537–12,544.

Molnar, P., and J. Stock (1987), Relative motions of hotspots in the Pacific, Atlantic and Indian Oceans since late Cretaceous time, *Nature*, *327*, 587–591.

Montelli, R., G. Nolet, F. A. Dahlen, G. Masters, E. R. Engdahl, and S. Hung (2004), Finite-frequency tomography reveals a variety of plumes in the mantle, *Science*, *303*, 338–343.

Morgan, W. J. (1971), Convection plumes in the lower mantle, *Nature*, *230*, 42–43.

Morgan, W. J. (1972), Deep mantle convective plumes and plate motions, *Am. Assoc. Pet. Geol. Bull.*, *56*, 203–213.

Morgan, W. J. (1978), Rodriguez, Darwin, Amsterdam—A second type of hotspot island, *J. Geophys. Res.*, *83*, 5355–5360.

Müller, R. D., and W. R. Roest (1992), Fracture zones in the North Atlantic from combined Geosat and Seasat data, *J. Geophys. Res.*, *97*(B3), 3337–3350.

Müller, R. D., J.-Y. Royer, and L. A. Lawver (1993), Revised plate motions relative to the hotspots from combined Atlantic and Indian Ocean hotspot tracks, *Geology*, *16*, 275–278.

Müller, R. D., W. R. Roest, and J.-Y. Royer (1998), Asymmetric seafloor spreading expresses ridge-plume interactions, *Nature*, *396*, 455–459.

Nicolaysen, K., F. A. Frey, K. Hodges, D. Weis, A. Giret, and H. Leyrit (1996), $^{40}Ar/^{39}Ar$ geochronology of flood basalts forming the Kerguelen Archipelago, *Eos Trans. AGU*, *77*(46), Fall. Meet. Suppl., F824.

Nürnberg, D., and R. D. Müller (1991), The tectonic evolution of the South Atlantic from Late Jurassic to present, *Tectonophysics*, *191*, 27–53.

O'Connor, J. M., and R. A. Duncan (1990), Evolution of the Walvis Ridge Rio Grande Rise hot spot system: Implications for African South American plate motions over plumes, *J. Geophys. Res.*, *95*, 17,475–17,502.

O'Connor, J. M., and A. P. le Roex (1992), South Atlantic hot spot-plume systems: 1. Distribution of volcanism in time and space, *Earth Planet. Sci. Lett.*, *113*, 343–364.

O'Connor, J. M., P. Stoffers, P. van den Bogaard, and M. McWilliams (1999), First seamount age evidence for significantly slower African plate motion since 19 to 30 Ma, *Earth Planet. Sci. Lett.*, *171*(4), 575–589.

Olson, P., and H. Singer (1985), Creeping plumes, *J. Fluid Mech.*, *158*, 511–531.

O'Neill, C., R. D. Mueller, and B. Steinberger (2003), Geodynamic implications of moving Indian Ocean hotspots, *Earth Planet. Sci. Lett.*, *215*(1–2), 151–168.

Raymond, C. A., J. Stock, and S. Cande (2000), Fast Paleogene motion of the Pacific hotspots from revised global plate circuit constraints, in *The History and Dynamics of Global Plate Motions*, *Geophys. Monogr. Ser.*, vol. 121, pp. 359–375, edited by M. A. Richards, R. G. Gordon, and R. D. van der Hilst, AGU, Washington, D. C.

Renne, P. R., K. Deckart, M. Ernesto, G. Feraud, and E. M. Piccirillo (1996a), Age of the Ponta Grossa dike swarm (Brazil), and implications to Parana flood volcanism, *Earth Planet. Sci. Lett.*, *144*(1–2), 199–211.

Renne, P. R., J. M. Glen, S. C. Milner, and R. A. Duncan (1996b), Age of Etendeka flood volcanism and associated intrusions in southwestern Africa, *Geology*, *24*(7), 659–662.

Ricard, Y., C. Vigny, and C. Froidevaux (1989), Mantle heterogeneities, geoid, and plate motion: A Monte Carlo inversion, *J. Geophys. Res.*, *94*, 13,739–13,754.

Richards, M. A., and R. W. Griffiths (1988), Deflection of plumes by mantle shear flow: Experimental results and a simple theory, *Geophys. J. Int.*, *94*, 367–376.

Royer, J.-Y., and T. Chang (1991), Evidence for relative motions between the Indian and Australian plates during the last 20 m.y. from plate tectonic reconstructions: Implications for the deformation of the Indo-Australian plate, *J. Geophys. Res.*, *96*(B7), 11,779–11,802.

Royer, J. Y., and R. G. Gordon (1997), The motion and boundary between the Capricorn and Australian plates, *Science*, *277*(5330), 1268–1274.

Royer, J.-Y., and D. T. Sandwell (1989), Evolution of the Eastern Indian Ocean since the Late Cretaceous: Constraints from Geosat altimetry, *J. Geophys. Res.*, *94*(B10), 13,755–13,782.

Royer, J.-Y., J. W. Pierce, and J. K. Weissel (1991), Tectonic constraints on hotspot formation of the Ninetyeast Ridge, *Ocean Drill. Program Initial Rep.*, *121*, 763–776.

Royer, J. Y., et al. (1992), Indian Ocean plate reconstructions since the Late Jurassic, in *Synthesis of Results From Scientific Drilling in the Indian Ocean*, *Geophys. Monogr. Ser.*, vol. 70, edited by R. A. Duncan et al., pp. 471–475, AGU, Washington, D. C.

Rundle, C. C., M. Brook, N. J. Snelling, P. H. Reynolds, and S. M. Barr (1974), Radiometric age determinations, *Initial Rep. Deep Sea Drill. Proj.*, *26*, 513–516.

Sandwell, D. T., and W. H. F. Smith (1997), Marine gravity anomaly from Geosat and ERS-1 satellite altimetry, *J. Geophys. Res.*, *102*, 10,039–10,054.

Shaw, P. R., and S. C. Cande (1990), High-resolution inversion for South Atlantic plate kinematic using joint altimeter and magnetic anomaly data, *J. Geophys. Res.*, *95*(B3), 2625–2644.

Sleep, N. H. (1990), Hotspots and mantle plumes: Some phenomenology, *J. Geophys. Res.*, *95*(B5), 6715–6736.

Smith, W. H. F., and D. T. Sandwell (1997), Global sea floor topography from satellite altimetry and ship depth soundings, *Science*, *277*(5334), 1956–1962.

Steinberger, B. (2000), Plumes in a convecting mantle: Models and observations for individual hotspots, *J. Geophys. Res.*, *105*(B5), 11,127–11,152.

Steinberger, B. (2002), Motion of the Easter hot spot relative to Hawaii and Louisville hot spots, *Geochem. Geophys. Geosyst.*, *3*(11), 8503, doi:10.1029/2002GC000334.

Steinberger, B., and R. J. O'Connell (1997), Changes of the earths rotation axis owing to advection of mantle density heterogeneities, *Nature*, *387*(6629), 169–173.

Steinberger, B., and R. J. O'Connell (1998), Advection of plumes in mantle flow: Implications for hotspot motion, mantle viscosity and plume distribution, *Geophys. J. Int.*, *132*(2), 412–434.

Steinberger, B., and R. J. O'Connell (2000), Effects of mantle flow on hotspot motion, in *The History and Dynamics of Global Plate Motions*, *Geophys. Monogr. Ser.*, vol. 121, edited by M. A. Richards, R. G. Gordon, and R. D. van der Hilst, pp. 377–398, AGU, Washington, D. C.

Steinberger, B., R. Sutherland, and R. J. O'Connell (2004), Prediction of Hawaiian-Emperor seamount locations from a revised model of global plate motion and mantle flow, *Nature*, *430*, 167–173.

Stewart, K., S. Turner, S. Kelley, C. Hawkesworth, L. Kirstein, and M. Mantovani (1996), 3-D, Ar-40–Ar-39 geochronology in the Parana continental flood basalt province, *Earth Planet. Sci. Lett.*, *143*(1–4), 95–109.

Storey, M., et al. (1992), Lower Cretaceous volcanic rocks on continental margins and their relationship to the Kerguelen

Plateau, *Proc. Ocean Drill. Program Sci. Results*, *120*, 33–53.

Su, W. J., R. L. Woodward, and A. M. Dziewonski (1994), Degree 12 model of shear velocity heterogeneity in the mantle, *J. Geophys. Res.*, *99*, 6945–6980.

Tarduno, J. A., and R. D. Cottrell (1997), Paleomagnetic evidence for motion of the Hawaiian Hotspot during formation of the Emperor Seamounts, *Earth Planet. Sci. Lett.*, *153*(3–4), 171–180.

Tarduno, J. A., and J. Gee (1995), Large-scale motion between Pacific and Atlantic hotspots, *Nature*, *378*(6556), 477–480.

Torsvik, T. H., and R. Van der Voo (2002), Refining Gondwana and Pangea palaeogeography: Estimates of Phanerozoic non-dipole (octupole) fields, *Geophys. J. Int.*, *151*(3), 771–794.

Tucholke, B. E., and N. C. Smoot (1990), Evidence for age and evolution of Corner seamounts and Great Meteor seamount chain from multibeam seamount chain from multibeam bathymetry, *J. Geophys. Res.*, *95*(B11), 17,555–17,569.

Van Fossen, M. C., and D. V. Kent (1992), Paleomagnetism of 122 Ma plutons in New England and the Mid-Cretaceous paleomagnetic field in North America: True polar wander or large-scale differential mantle motion?, *J. Geophys. Res.*, *97*(B13), 19,651–19,661.

Vandamme, D., and V. Courtillot (1990), Paleomagnetism of Leg 115 basement rocks and latitudinal evolution of the Reunion hotspot, *Proc. Ocean Drill. Program Sci. Results*, *115*, 111–118.

Weis, D., S. Ingle, D. Damasceno, F. A. Frey, K. E. Nicolaysen, and J. Barling (2001), Origin of continental components in Indian Ocean basalts: Evidence from Elan Bank (Kerguelen Plateau, ODP Leg 183, site 1137), *Geology*, *29*(2), 147–150.

Weis, D., F. A. Frey, R. Schlich, M. Schaming, R. Montigny, D. Damasceno, N. Mattielli, K. E. Nicolaysen, and J. S. Scoates (2002), Trace of the Kerguelen mantle plume: Evidence from seamounts between the Kerguelen Archipelago and Heard Island, Indian Ocean, *Geochem. Geophys. Geosyst.*, *3*(6), 1033, doi:10.1029/2001GC000251.

Wessel, P., and L. W. Kroenke (1997), A geometric technique for relocating hotspots and refining absolute plate motions, *Nature*, *387*, 365–369.

Wigand, M., A. K. Schmitt, R. B. Trumbull, I. M. Villa, and R. Emmermann (2004), Short-lived magmatic activity in an anorogenic subvolcanic complex: ^{40}Ar/^{39}Ar and ion microprobe U-Pb zircon dating of the Erongo, Damaraland, Namibia, *J. Volcanol. Geotherm. Res.*, *130*, 285–305.

Wolfe, C. J., I. T. Bjarnason, J. C. VanDecar, and S. C. Solomon (1997), Seismic structure of the Iceland mantle plume, *Nature*, *385*(6613), 245–247.